

Pursuing Truth: Improving Retrievals on Mid-Infrared Exo-Earth Spectra with Physically Motivated Water Abundance Profiles and Cloud Models.

BJÖRN S. KONRAD ^{1,2} SASCHA P. QUANZ ^{1,2,3} ELEONORA ALEI ⁴ AND ROBIN WORDSWORTH ^{5,6}

¹*ETH Zurich, Institute for Particle Physics and Astrophysics, Wolfgang-Pauli-Strasse 27, CH-8093 Zurich, Switzerland*

²*National Center of Competence in Research PlanetS, Gesellschaftsstrasse 6, CH-3012 Bern, Switzerland*

³*ETH Zurich, Department of Earth Sciences, Sonneggstrasse 5, 8092 Zurich, Switzerland*

⁴*NASA Postdoctoral Program Fellow, NASA Goddard Space Flight Center, Greenbelt, MD, USA*

⁵*School of Engineering and Applied Sciences, Harvard University, Cambridge, MA 02138, USA*

⁶*Department of Earth and Planetary Sciences, Harvard University, Cambridge, MA 02138, USA*

(Received 06.06.2024; Revised 16.08.2024; Accepted 27.08.2024)

Submitted to ApJ

ABSTRACT

Atmospheric retrievals are widely used to constrain exoplanet properties from observed spectra. We investigate how the common nonphysical retrieval assumptions of vertically constant molecule abundances and cloud-free atmospheres affect our characterization of an exo-Earth (an Earth-twin orbiting a Sun-like star). Specifically, we use a state-of-the-art retrieval framework to explore how assumptions for the H₂O profile and clouds affect retrievals. In a first step, we validate different retrieval models on a low-noise simulated 1D mid-infrared (MIR) spectrum of Earth. Thereafter, we study how these assumptions affect the characterization of Earth with the Large Interferometer For Exoplanets (LIFE). We run retrievals on LIFE mock observations based on real disk-integrated MIR Earth spectra. The performance of different retrieval models is benchmarked against ground truths derived from remote sensing data. We show that assumptions for the H₂O abundance and clouds directly affect our characterization. Overall, retrievals that use physically motivated models for the H₂O profile and clouds perform better on the empirical Earth data. For observations of Earth with LIFE, they yield accurate estimates for the radius, pressure-temperature structure, and the abundances of CO₂, H₂O, and O₃. Further, at $R = 100$, a reliable and bias-free detection of the biosignature CH₄ becomes feasible. We conclude that the community must use a diverse range of models for temperate exoplanet atmospheres to build an understanding of how different retrieval assumptions can affect the interpretation of exoplanet spectra. This will enable the characterization of distant habitable worlds and the search for life with future space-based instruments.

Keywords: Earth (planet) — Biosignatures — Exoplanet atmospheric variability — Astrobiology — Infrared spectroscopy — Atmospheric retrievals — Space vehicles instruments

1. INTRODUCTION

Both the Astrobiology Strategy (Hays et al. 2017) and the Astro 2020 Decadal Survey in the United States (National Academies of Sciences, Engineering, and Medicine 2021) identify the atmospheric characterization of terrestrial exoplanets as a key endeavor for exoplanet science. The measurement and subsequent analysis of an exoplanet’s spectrum

allows us to constrain key atmospheric properties such as the pressure-temperature (P – T) structure and the molecular composition. Such constraints shed light on the planet’s habitability and could enable the detection of biological activity.

Temperate exoplanets with Earth-like radii and masses that reside within their host star’s habitable zone (HZ; Kasting et al. 1993; Kopparapu et al. 2013) are of particular interest. Findings from transit surveys such as the Kepler mission (Borucki et al. 2010) or the Transiting Exoplanet Survey Satellite (TESS; Ricker et al. 2015) and current long-term radial velocity (RV) surveys predict that these planets are a common occurrence (e.g., Petigura et al. 2013; Foreman-

Mackey et al. 2014; Dressing & Charbonneau 2015; Bryson et al. 2021). Several rocky HZ exoplanets have been found within 20 pc of the sun (see, e.g., Hill et al. 2023, for a catalogue) via both the transit (e.g., Berta-Thompson et al. 2015; Gillon et al. 2017; Vanderspek et al. 2019) and the RV (e.g., Anglada-Escudé et al. 2016; Ribas et al. 2016; Zechmeister et al. 2019) methods. Currently, transit observations with the James Webb Space Telescope (JWST) are investigating whether rocky exoplanets orbiting M dwarf stars can retain significant atmospheres (e.g., Koll et al. 2019; Greene et al. 2023; Zieba et al. 2023; Lustig-Yaeger et al. 2023b; Ih et al. 2023; Lincowski et al. 2023; Madhusudhan et al. 2023; Lim et al. 2023). Yet, the JWST will likely not provide a detailed atmospheric characterization of these objects (e.g., Morley et al. 2017; Krissansen-Totton et al. 2018). In the near future, ground-based extremely large telescopes (ELTs) will directly measure the reflected stellar light and thermal emission of the closest HZ exoplanets (e.g., Quanz et al. 2015; Bowens et al. 2021; Kasper et al. 2021). However, a detailed atmospheric characterization for a statistically significant number (dozens) of rocky HZ exoplanets is not achievable by any current or approved future instrument.

Thus, the exoplanet community is pushing for a next generation of space-based observatories. Motivated by the LUVOIR (The LUVOIR Team 2019) and HabEx (Gaudi et al. 2020) mission concepts, The Astro 2020 Decadal Survey in the United States (National Academies of Sciences, Engineering, and Medicine 2021) recommended the space-based Habitable Worlds Observatory (HWO). HWO aims to directly detect host-star light scattered by rocky HZ exoplanets in the ultraviolet, optical, and near-infrared (UV/O/NIR) wavelength range. Yet, an exoplanet’s mid-infrared (MIR) thermal emission spectrum also encodes unique information about the atmospheric state and the surface conditions (e.g., Des Marais et al. 2002; Hearty et al. 2009; Catling et al. 2018; Schwieterman et al. 2018; Mettler et al. 2020; Mettler et al. 2023). Thus, the direct detection of the thermal emission of rocky, temperate exoplanets in the MIR has been identified as one of the most important science topics to be considered for the future science program of the European Space Agency (ESA) (Voyage 2050 Senior Committee 2021). This was triggered by a White Paper submitted by members of the Large Interferometer For Exoplanets (LIFE) initiative (Quanz et al. 2021), which is working on developing a large space-based MIR nulling interferometer (Kammerer & Quanz 2018; Quanz et al. 2022).

Several studies have investigated the LIFE instrument design (Dannert et al. 2022; Hansen et al. 2022, 2023; Matsuo et al. 2023) and its potential to detect rocky HZ exoplanets (Quanz et al. 2022; Kammerer et al. 2022; Carrión-González et al. 2023). Further studies focused on LIFE’s potential to characterize terrestrial exoplanets by studying simulated 1D

spectra. Konrad et al. (2022) derived first constraints for the wavelength coverage, spectral resolving power (R), and signal-to-noise (S/N) levels by studying a cloud-free modern Earth. Subsequent studies reevaluated these requirements by analyzing Earth at different epochs of its evolution (Alei et al. 2022b), a cloudy Venus (Konrad et al. 2023), and the detectability of biosignature gases (Angerhausen et al. 2023, 2024). Last, Alei et al. (2024) investigated how combined observations of an Earth-twin with HWO and LIFE could improve its characterization. Thereby, the uniqueness of the information attainable from a planet’s MIR emission is highlighted.

These LIFE studies all analyze spectra that were generated using a 1D atmosphere model. However, Mettler et al. (2020) find significant discrepancies between thermal emission spectra from different locations on Earth. In Mettler et al. (2023), real disk-integrated rather than local Earth MIR emission spectra are analyzed. The authors find that Earth’s MIR emission depends significantly on the observed viewing geometry and season. Thus, a representative, disk-integrated MIR spectrum does not exist for Earth. In a third study, Mettler et al. (2024) treat Earth as an exoplanet observed with LIFE. By running atmospheric retrievals on empirical MIR disk-integrated spectra from Earth observing satellites, the authors study how their characterization of Earth depends on the viewing angle and season. They conclude that viewing geometry and season only minorly impact their results and successfully characterize Earth as a temperate habitable planet, featuring biosignature gases.

However, when comparing the retrieved parameter estimates with remote sensing ground truth data, Mettler et al. (2024) observe significant offsets between the two. The authors predominantly attribute these biases to two simplifying retrieval assumptions. First, their retrieval model assumes all abundance profiles to be constant throughout the atmosphere. Especially for the strong MIR absorber H_2O , whose abundance varies by several orders of magnitude throughout Earth’s atmosphere, this is a strong simplification. Second, they neglect Earth’s patchy cloud coverage by assuming a cloud-free atmosphere in all retrieval models.

The main aim of this study is to demonstrate that simple physical models for the H_2O structure and the clouds in Earth’s atmosphere can significantly reduce such biases. First, we validate our models with retrievals on simulated 1D Earth spectra. Later, we run retrievals on the same empirical disk-integrated Earth spectra considered in Mettler et al. (2024) and compare the results with ground truth remote sensing data. Such studies on real observations of terrestrial solar system planets are uncommon (e.g., Tinetti et al. 2006; Robinson & Salvador 2023; Lustig-Yaeger et al. 2023a). Yet, they provide a powerful approach to help us understand how common retrieval assumptions can bias our results. Build-

ing this understanding is indispensable to ensure the correct characterization of terrestrial HZ exoplanets in the future.

2. DATASETS AND METHODS

Here, we introduce our retrieval routine and the datasets studied. In Section 2.1, we provide information on the retrieval routine and our models for the H₂O abundance profile and clouds. Next, in Section 2.2, we introduce the three different retrieval forward models considered. Last, we introduce the different input spectra and noise models, and justify the assumed priors in Sections 2.3 and 2.4.

2.1. Atmospheric retrieval routine

We run retrievals using a modified version of the retrieval routine initially introduced in Konrad et al. (2022) and later improved and modified in Alei et al. (2022b) and Konrad et al. (2023). Here, we provide a brief summary of the original routine and focus on the additions to the routine made for this publication. For an in-depth description of the retrieval framework, we refer to the original publications.

The retrieval framework is based on the radiative transfer code `petitRADTRANS` (Mollière et al. 2019, 2020; Alei et al. 2022b), which is used to calculate the theoretical MIR thermal emission spectrum of a 1D plane-parallel parametric atmosphere model. The model atmosphere is defined via a set of forward model parameters (see Section 2.2 for a description of the forward models we used). To calculate the MIR emission spectrum corresponding to a set of model parameters, `petitRADTRANS` assumes the planetary surface to emit black-body radiation. It then models the interaction of each discrete atmospheric layer with the radiation by accounting for absorption, emission, and scattering. This yields the MIR flux at the top of the atmosphere.

The goal of a retrieval is to search the space spanned by the forward model parameters for combinations of parameter values that best reproduce an observed planet spectrum. The prior probability distributions (or “priors”) of the model parameters specify the parameter space to be probed by the retrieval. To efficiently explore this prior space, we use `pyMultiNest` (Buchner et al. 2014), a python package based on the `MultiNest` (Feroz et al. 2009) implementation of Nested Sampling (Skilling 2006). For this study, we ran all retrievals using 700 live points and a sampling efficiency of 0.3¹.

The output of a retrieval are posterior probability distributions (or “posteriors”) for the model parameters. The posteriors summarize how likely different combinations of parameter values are. In addition, our retrieval routine yields estimates of the Bayesian evidence \mathcal{Z} , which quantifies how well the forward model fits the input spectrum. Thus, \mathcal{Z} pro-

Table 1. Jeffreys scale (Jeffreys 1998).

$\log_{10}(K)$	Probability	Strength of Evidence
< 0	< 0.5	Support for \mathcal{B}
$0 - 0.5$	$0.5 - 0.75$	Very weak support for \mathcal{A}
$0.5 - 1$	$0.75 - 0.91$	Substantial support for \mathcal{A}
$1 - 2$	$0.91 - 0.99$	Strong support for \mathcal{A}
> 2	> 0.99	Decisive support for \mathcal{A}

NOTE—Scale to interpret the Bayes’ factor K for two models \mathcal{A} and \mathcal{B} . The scale is symmetrical, i.e., negative values of $\log_{10}(K)$ correspond to very weak, substantial, strong, or decisive support for model \mathcal{B} .

vides a means of comparing the performance of different forward models. If we run two retrievals on the same spectrum using different forward models \mathcal{A} and \mathcal{B} , the retrievals will yield different log-evidences $\ln(\mathcal{Z}_{\mathcal{A}})$ and $\ln(\mathcal{Z}_{\mathcal{B}})$. From the log-evidences, we calculate the Bayes’ factor K :

$$\log_{10}(K) = \frac{\ln(\mathcal{Z}_{\mathcal{A}}) - \ln(\mathcal{Z}_{\mathcal{B}})}{\ln(10)}. \quad (1)$$

The value of K specifies which model is preferred. A positive $\log_{10}(K)$ marks a preference for model \mathcal{A} , whereas negative values indicate preference for \mathcal{B} . The Jeffreys scale (Jeffreys 1998, Table 1) provides a quantification for the strength of the model preference.

2.1.1. Model for water condensation

Retrievals commonly assume that the atmospheric trace-gas abundances are vertically constant. While this assumption helps reduce the computational complexity, recent studies have shown that it can bias the retrieved posteriors (e.g., Rowland et al. 2023). For Earth, H₂O has strong spectral features throughout the MIR (e.g., Figure 1 in Konrad et al. 2022). The bulk of Earth’s MIR emission originates from the lowermost atmospheric layers (between 1 bar and 0.1 bar), where the atmospheric H₂O content decreases strongly with altitude by more than 3 orders of magnitude (see, e.g., Figure 1; Mettler et al. 2024). The main process responsible for this decrease in H₂O in Earth’s lower atmosphere is the convection of moist air from the surface to higher atmospheric layers. The rising moist air cools causing H₂O to condense, form clouds, and rain out. Consequentially, the H₂O abundance drops significantly with altitude in Earth’s atmosphere, and we expect signatures thereof to be imprinted in the MIR emission.

To model the condensation induced vertical variations in the H₂O profile in our retrieval forward model, we start by

¹ As suggested for evidence evaluation by the `MultiNest` documentation: <https://github.com/farhanferoz/MultiNest>.

calculating the saturation vapor pressure of H_2O for each atmospheric layer. For this, we use the temperature T of the layer as well as one of the two experimentally determined Goff-Gratch equations (Eqs. 2 and 3; Goff & Gratch 1946; Goff 1957). If T is greater than the triple point temperature of H_2O ($T_{\text{tp}} = 273.16 \text{ K}$), we use the equation for the saturation vapor pressure over water ($p_{v, \text{water}}$ in hPa):

$$\begin{aligned} p_{v, \text{water}}(T) = & l_1 \cdot (1 - T_{\text{st}}/T) + l_2 \cdot \log_{10}(T_{\text{st}}/T) \\ & + l_3 \cdot 10^{-7} \cdot (1 - 10^{l_4 \cdot (1-T/T_{\text{st}})}) \\ & + l_5 \cdot 10^{-3} \cdot (10^{l_6 \cdot (1-T_{\text{st}}/T)} - 1) + \log_{10}(p_{\text{st}}). \end{aligned} \quad (2)$$

Here, $T_{\text{st}} = 373.15 \text{ K}$ and $p_{\text{st}} = 1013.25 \text{ hPa}$ are the steam-point temperature and pressure of H_2O , and the factors l_i are constants: $l_1 = 7.90298$, $l_2 = 5.02808$, $l_3 = 1.3816$, $l_4 = 11.344$, $l_5 = 8.1328$, and $l_6 = 3.49149$. Conversely, if T lies below T_{tp} , we use the Goff-Gratch equation for the saturation vapor pressure over ice ($p_{v, \text{ice}}$ in hPa):

$$\begin{aligned} p_{v, \text{ice}}(T) = & s_1 \cdot (1 - T_{\text{tp}}/T) - s_2 \cdot \log_{10}(T_{\text{tp}}/T) \\ & + s_3 \cdot (1 - T/T_{\text{tp}}) + \log_{10}(p_{\text{tp}}). \end{aligned} \quad (3)$$

Here, $p_{\text{tp}} = 6.1173 \text{ hPa}$ is the triple point pressure of H_2O , and the factors s_i are constants: $s_1 = 9.09718$, $s_2 = 3.56654$, and $s_3 = 0.876793$. The vapor pressure of H_2O (p_v) as a function of T can be summarized as:

$$p_v(T) = \begin{cases} p_{v, \text{water}}(T), & \text{if } T \geq T_{\text{tp}}, \\ p_{v, \text{ice}}(T), & \text{otherwise.} \end{cases} \quad (4)$$

Next, we assume a vertically constant volume mixing ratio of H_2O ($\nu_{\text{H}_2\text{O}}$). Starting from the surface layer, we follow the atmospheric P - T structure to the higher atmospheric layers with pressures p and temperatures T . For each layer, we compare the partial pressure of H_2O ($p_{\text{H}_2\text{O}} = \nu_{\text{H}_2\text{O}} \cdot p$) to $p_v(T)$. If $p_{\text{H}_2\text{O}}$ lies below $p_v(T)$, we proceed to the next layer. In contrast, if $p_{\text{H}_2\text{O}}$ in a layer exceeds $p_v(T)$, we reduce $\nu_{\text{H}_2\text{O}}$ in that layer and all lower-pressure layers such that $p_{\text{H}_2\text{O}}$ in the current layer equals $p_v(T)$. This yields a $\nu_{\text{H}_2\text{O}}(p)$ profile that is either constant or decreasing with altitude (depending on the P - T structure and $\nu_{\text{H}_2\text{O}}$ in the surface layer).

This condensation model accurately estimates $\nu_{\text{H}_2\text{O}}(p)$ in Earth's lower troposphere ($p > 0.3 \text{ bar}$), where $p_{\text{H}_2\text{O}}$ is comparable to $p_v(T)$. However, it significantly overestimates the $\nu_{\text{H}_2\text{O}}(p)$ in Earth's dry upper troposphere and stratosphere ($p < 0.3 \text{ bar}$), where $p_{\text{H}_2\text{O}}$ is significantly smaller than $p_v(T)$. In our retrievals, we allow for a dry upper atmosphere by adding a drying parameter, $\delta_{\text{H}_2\text{O}} \in [0, 1]$, to the forward model. Using the parameter $\delta_{\text{H}_2\text{O}}$, we calculate the dried H_2O profile, $\nu_{\text{H}_2\text{O}, \text{dry}}(p)$, as follows:

$$\nu_{\text{H}_2\text{O}, \text{dry}}(p) = \nu_{\text{H}_2\text{O}}(p) \cdot \delta_{\text{H}_2\text{O}}^{\nu_{\text{H}_2\text{O}, \text{TOA}}/\nu_{\text{H}_2\text{O}}(p)}. \quad (5)$$

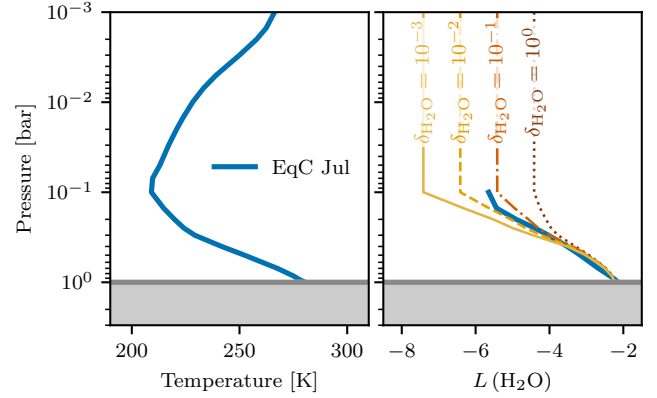


Figure 1. H_2O profiles calculated using the condensation model (Section 2.1.1) for the EqC Jul Earth view (Section 2.3.2). *Left panel:* The ground truth P - T profile for the EqC Jul view of Earth. *Right panel:* The ground truth H_2O profile as a thick blue line together with the H_2O profiles calculated for different $\delta_{\text{H}_2\text{O}}$ values.

Here, $\nu_{\text{H}_2\text{O}, \text{TOA}}$ is $\nu_{\text{H}_2\text{O}}(p)$ in the uppermost atmospheric layer. Equation 5 is designed such that the drying is strongest for small values of $\delta_{\text{H}_2\text{O}}$ and for atmospheric layers where $\nu_{\text{H}_2\text{O}}(p)$ is comparable to $\nu_{\text{H}_2\text{O}, \text{TOA}}$. A value of $\delta_{\text{H}_2\text{O}} = 1$ results in $\nu_{\text{H}_2\text{O}, \text{dry}}(p) = \nu_{\text{H}_2\text{O}}(p)$, which means that there is no drying in the upper atmosphere.

In Figure 1, we demonstrate that our condensation model yields realistic estimates for Earth's H_2O profile. We compare the ground truth H_2O profile for the disk-integrated average equatorial view of Earth in July (EqC Jul) with H_2O profiles that we calculated from the EqC Jul P - T structure using our condensation model and different $\delta_{\text{H}_2\text{O}}$ values (see Section 2.3.2 for information on the EqC Jul view). We observe that our condensation model successfully approximates Earth's true H_2O profile for $\delta_{\text{H}_2\text{O}} = 10^{-1} - 10^{-2}$. The value of $\delta_{\text{H}_2\text{O}}$ mainly affects the H_2O profile for $p < 0.3 \text{ bar}$ and is required to accurately model Earth's H_2O structure. If drying is neglected (brown-dotted line; $\delta_{\text{H}_2\text{O}} = 10^0$), we fail to accurately reproduce Earth's H_2O profile.

2.1.2. Model for partial cloud coverage

The condensation of H_2O in Earth's atmosphere is linked to the formation of H_2O clouds. Thus, if H_2O condenses in our model atmosphere, we expect clouds to form. To account for this effect, we add the option to include a simple model for partial cloud coverage in the retrieval forward model.

To account for clouds in our retrievals, we position gray clouds at an atmospheric pressure of p_C . We calculate p_C by taking the median pressure of all atmosphere layers where H_2O condensation occurs that exhibit a relative humidity greater than 10% (i.e., $p_{\text{H}_2\text{O}}(p)/p_v(T) > 0.1$). This assumption for p_C positions the clouds within the atmospheric layers where H_2O condenses. If no H_2O condensation occurs, we assume the atmosphere to be cloud-free.

To model an Earth-like partial cloud cover, we use our retrieval forward model to calculate the spectra for a cloud-free (F_{CF}) and cloudy (F_{C}) model atmosphere. We then mix the two spectra as follows to obtain the total flux F_{tot} as a function of the wavelength λ :

$$F_{\text{tot}}(\lambda) = f_{\text{C}} \cdot F_{\text{C}}(\lambda) + (1 - f_{\text{C}}) \cdot F_{\text{CF}}(\lambda). \quad (6)$$

Here, the forward model parameter $f_{\text{C}} \in [0, 1]$ describes the cloud-fraction. A value of $f_{\text{C}} = 0$ corresponds to the cloud-free case, whereas $f_{\text{C}} = 1$ yields a fully cloudy atmosphere.

2.2. Retrieval forward models

We run retrievals using the three different forward models listed in Table 2. A complete list of the parameters used by each model is provided in Table 3. All models assume a 1D atmosphere consisting of 100 equally thick layers (in log-space) between 10^{-4} bar and the surface pressure P_0 . Each individual layer is characterized by its pressure P , the corresponding temperature T , and the opacity sources present. As in Konrad et al. (2022, 2023), Alei et al. (2022b, 2024), and Mettler et al. (2024), we parameterize the atmospheric P - T structure by means of a fourth order polynomial:

$$T(P) = \sum_{i=0}^4 a_i P^i. \quad (7)$$

The factors a_i are the five forward model parameters describing the atmospheric P - T structure. This choice is motivated by Konrad et al. (2022), who demonstrate that a polynomial P - T model helps reduce a retrieval’s computational complexity by minimizing the number of P - T parameters².

Further, all models assume the same spectroscopically active molecules to be present. We model MIR molecular absorption and emission features of CO_2 , H_2O , O_3 , and CH_4 ³. The used line lists, broadening coefficients, and cutoffs are summarized in Table 4. We also consider collision-induced absorption (CIA) and Rayleigh scattering features of atmospheric molecules (all considered CIA-pairs and Rayleigh-species are summarized in Table 4). Further, we use a spectroscopically inactive filling gas with the mean molecular weight of N_2 to ensure that: $\sum(\text{gas abundances}) = 1$. Last, to determine the scale height of the model atmosphere, we require the planetary surface gravity, which we calculate from the radius and mass parameters (R_{pl} , M_{pl}).

² In a recent publication, Gebhard et al. (2023) demonstrated that learning-based P - T models can reduce the number of P - T parameters further. However, the accuracy of such models for terrestrial P - T structures is currently limited by the availability of sufficient training data.

³ This choice of molecules is motivated by a detailed Bayesian model comparison study performed by Mettler et al. (2024) for the same disk-integrated Earth spectra.

The three forward models only differ in the assumptions made for the H_2O abundance profile and the clouds. The simplest model ($\mathcal{M}_{\text{C,CF}}$) assumes constant abundance profiles for all molecules and a cloud-free atmosphere. This model is equivalent to the forward model used in Mettler et al. (2024). The intermediate complexity model ($\mathcal{M}_{\text{V,CF}}$) again assumes the atmosphere to be cloud-free. However, it allows for a non-constant H_2O abundance profile by modeling H_2O condensation as described in Section 2.1.1. The most complex of the three models ($\mathcal{M}_{\text{V,CL}}$) also accounts for H_2O condensation. In addition, it relaxes the assumption of a cloud-free atmosphere by modeling partial cloud coverage following the method outlined in Section 2.1.2.

2.3. Input spectra for the retrievals

In the context of this study, we consider two different types of input spectra. All considered spectra are characterized by their spectral resolving power (R) and signal-to-noise ratio (S/N). We define the R of a spectrum as $\lambda/\Delta\lambda$, where $\Delta\lambda$ is the width of a given wavelength bin and λ the wavelength at the bin’s center. We introduce the simulated 1D Earth spectrum used to test the different forward models in Section 2.3.1. Next, in Section 2.3.2, we provide information on the empirical, disk-integrated Earth spectra and the corresponding ground truths studied in the main analysis of this work. Last, we provide details on the assumptions made for the wavelength dependent S/N of all spectra in Section 2.3.3.

2.3.1. Simulated 1D Earth spectrum

Before performing retrievals on real, disk-integrated Earth spectra, we run test retrievals with all forward models on a simulated spectrum of a 1D Earth-like atmosphere to validate our approach. We generate the 1D Earth spectrum using the cloudy $\mathcal{M}_{\text{V,CL}}$ forward model (see Section 2.2). We assume an Earth-like P - T structure, radius, mass, and atmospheric composition (see Table 3 and Figure 2). The atmospheric H_2O content is determined with the condensation model by assuming $\delta_{\text{H}_2\text{O}} = 10^{-2}$. For the cloud fraction, we assume $f_{\text{C}} = 0.67$, which corresponds to the lower limit for the mean annual cloud fractions of the Earth views in Mettler et al. (2024) (range: $f_{\text{C}} = 0.67 - 0.71$). We calculate the spectrum for the minimal LIFE wavelength range (4 – 18.5 μm) specified in Konrad et al. (2022), choose a spectral resolving power of $R = 100$, and assume $S/N = 20$ photon-noise (low-noise model in Section 2.3.3). We show the obtained simulated MIR Earth spectrum in the bottom panel of Figure 2.

2.3.2. Real disk-integrated Earth spectra and ground truths

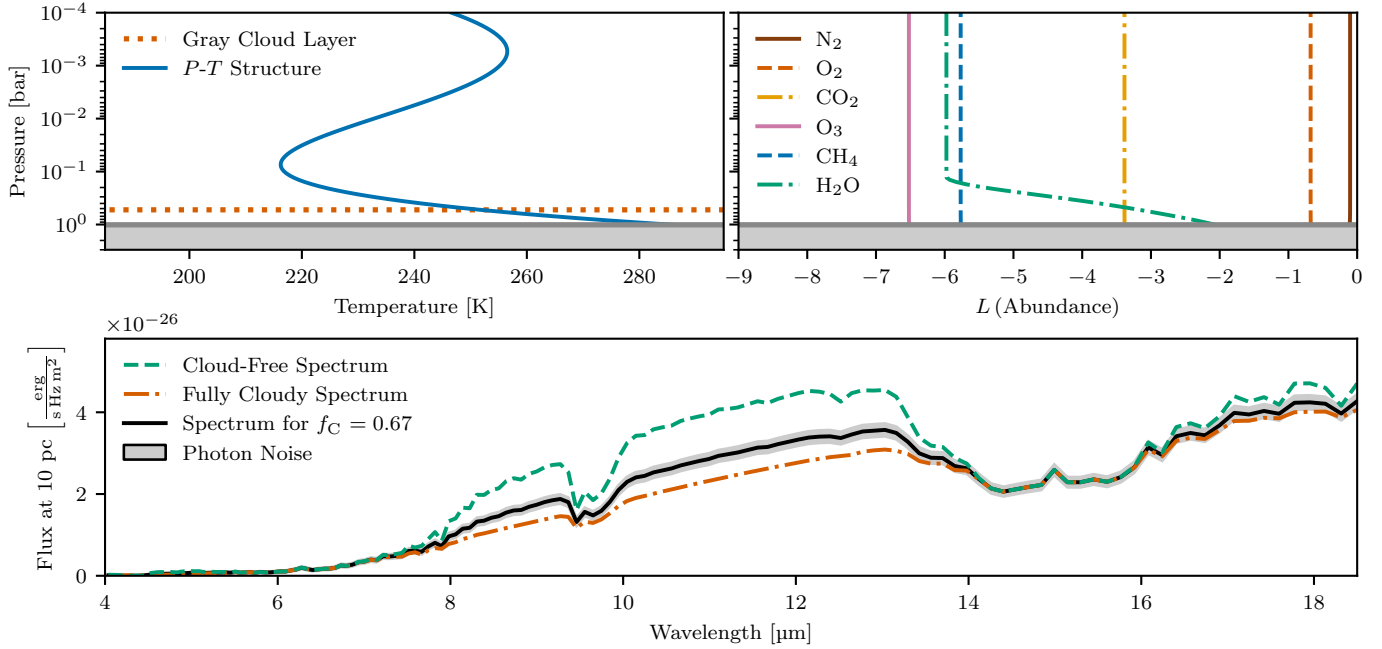


Figure 2. P - T and abundance profiles assumed for the simulated Earth input spectrum (Section 2.3.1). *Top-left panel:* Assumed Earth-like P - T structure (solid blue line) and position of the cloud layer (dotted red line). *Top-right panel:* Vertical profiles of the considered atmospheric gases. *Bottom panel:* Calculated cloud-free (dashed green line), cloudy (dashed-dotted red line), and partially cloudy ($f_C = 0.67$; solid black line) Earth spectra. The gray-shaded area indicates the $S/N = 20$ photon noise level assumed for the partially cloudy input spectrum.

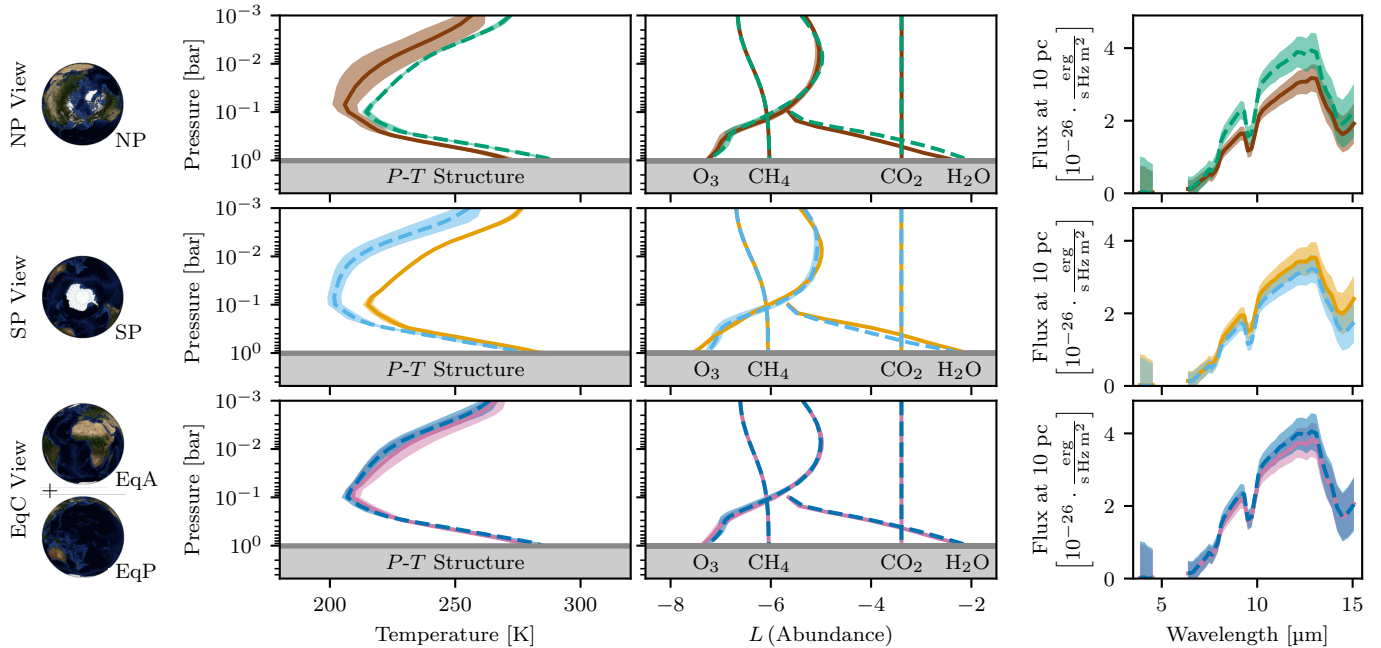
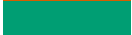


Figure 3. Ground truths and disk-integrated MIR spectra for the NP, SP, and EqC Earth views introduced in Section 2.3.2. Solid lines indicate the data for January and dashed lines represent the month July. Color-shaded areas indicate the uncertainties on the data. *Left column:* Ground truth P - T profiles. *Center column:* Ground truth abundance profiles for CO_2 , O_3 , CH_4 , and H_2O . *Right column:* $R = 50$ disk-integrated monthly averaged Earth spectra. The color-shaded areas indicate the $S/N = 10$ LIFESIM-noise level.

Table 2. Summary of the three different retrieval forward models.

Model	Color-coding	Model description
$\mathcal{M}_{C,CF}$		Vertically constant H ₂ O abundance, cloud-free
$\mathcal{M}_{V,CF}$		H ₂ O abundance from condensation model, cloud-free
$\mathcal{M}_{V,CL}$		H ₂ O abundance from condensation model, partial cloud coverage

NOTE—The second column shows the color-coding used for the models throughout this publication.

Table 3. Model parameters, values for the validation retrieval, priors, and model configurations.

Parameter	Description	Validation True Values	Prior	Model Configuration		
				$\mathcal{M}_{C,CF}$	$\mathcal{M}_{V,CF}$	$\mathcal{M}_{V,CL}$
a_4	P - T parameter (degree 4)	1.69	$\mathcal{U}(0, 10)$	✓	✓	✓
a_3	P - T parameter (degree 3)	23.12	$\mathcal{U}(0, 100)$	✓	✓	✓
a_2	P - T parameter (degree 2)	99.70	$\mathcal{U}(0, 500)$	✓	✓	✓
a_1	P - T parameter (degree 1)	146.63	$\mathcal{U}(0, 500)$	✓	✓	✓
a_0	P - T parameter (degree 0)	285.22	$\mathcal{U}(0, 1000)$	✓	✓	✓
$L(P_0)$	L (Surface pressure [bar])	0.01	$\mathcal{U}(-4, 2)$	✓	✓	✓
R_{pl}	Planet radius [R_{\oplus}]	1.00	$\mathcal{G}(1.0, 0.2)$	✓	✓	✓
$L(M_{pl})$	L (Planet mass [M_{\oplus}])	0.00	$\mathcal{G}(0.0, 0.4)$	✓	✓	✓
$L(N_2)$	L (N ₂ mass fraction)	-0.10	$\mathcal{U}(-10, 0)$	✓	✓	✓
$L(O_2)$	L (O ₂ mass fraction)	-0.68	$\mathcal{U}(-10, 0)$	✓	✓	✓
$L(CO_2)$	L (CO ₂ mass fraction)	-3.39	$\mathcal{U}(-10, 0)$	✓	✓	✓
$L(O_3)$	L (O ₃ mass fraction)	-6.52	$\mathcal{U}(-10, 0)$	✓	✓	✓
$L(CH_4)$	L (CH ₄ mass fraction)	-5.77	$\mathcal{U}(-10, 0)$	✓	✓	✓
$L(H_2O)$	L (H ₂ O mass fraction)	-2.10	$\mathcal{U}(-10, -1)$	✓	✓	✓
$L(\delta_{H_2O})$	L (H ₂ O drying parameter)	-2.00	$\mathcal{U}(-5, 0)$	✗	✓	✓
f_C	Cloud fraction	0.67	$\mathcal{U}(0, 1)$	✗	✗	✓

NOTE—Here, $L(\cdot)$ stands for $\log_{10}(\cdot)$. In the third column we specify the values assumed to generate the mock-Earth spectrum for the validation retrievals. The listed H₂O value is the abundance at the surface obtained from the condensation model. The f_C value is motivated by the average cloud fractions presented in [Mettler et al. \(2024\)](#) and δ_{H_2O} is chosen such that the calculated H₂O profile fits Earth's profile. All other parameter values are taken from [Konrad et al. \(2022\)](#). In the fourth column, the assumed priors are listed. We denote a boxcar prior with lower threshold x and upper threshold y as $\mathcal{U}(x, y)$; For a Gaussian prior with mean μ and standard deviation σ , we write $\mathcal{G}(\mu, \sigma)$. The last three columns summarize the model parameters used by the different retrieval forward models (✓ = used, ✗ = unused).

Table 4. Line and continuum opacities used for this study.

Molecular Line Opacities				CIA		Rayleigh Scattering	
Molecule	Line List	Pressure-broadening	Wing cutoff	Pair	Reference	Molecule	Reference
CO ₂	HN20	γ_{air}	25 cm ⁻¹	N ₂ -N ₂	KA19	N ₂	TH14, TH17
H ₂ O	HN20	γ_{air}	25 cm ⁻¹	N ₂ -O ₂	KA19	O ₂	TH14, TH17
O ₃	HN20	γ_{air}	25 cm ⁻¹	O ₂ -O ₂	KA19	CO ₂	SU05
CH ₄	HN20	γ_{air}	25 cm ⁻¹	CO ₂ -CO ₂	KA19	CH ₄	SU05
...	CH ₄ -CH ₄	KA19	H ₂ O	HA98
...	H ₂ O-H ₂ O	KO21
...	H ₂ O-N ₂	KO21

References—(HA98) [Harvey et al. \(1998\)](#); (HN20) [Gordon et al. \(2022\)](#); (KA19) [Karman et al. \(2019\)](#); (KO21) [Kofman & Villanueva \(2021\)](#); (SU05) [Sneep & Ubachs \(2005\)](#); (TH14) [Thalman et al. \(2014\)](#); (TH17) [Thalman et al. \(2017\)](#).

As input for the main retrieval analysis of this study, we use the same set of monthly averaged⁴ disk-integrated Earth spectra as in [Mettler et al. \(2024\)](#). The spectra are derived from Earth remote sensing climate data from NASA’s Atmospheric Infrared Sounder (AIRS; [Chahine et al. 2006](#)) aboard the Aqua satellite. We refer to [Mettler et al. \(2023\)](#) and [Mettler et al. \(2024\)](#) for a description of the methods used to derive these disk-integrated, monthly averaged Earth spectra.

The spectra cover the 3.75 – 15.4 μm wavelength range, with a gap at 4.6 – 6.2 μm due to dead instrument channels. We consider three different orientations of Earth relative to the observer. For the North (NP) and South Pole (SP) case, the respective polar region is centered on the observed disk. The Equatorial Combined (EqC) view is centered on Earth’s equator and is the combination of an Africa-centered (EqA) and a Pacific-centered (EqP) equatorial view. We combine the EqA and EqP views into the EqC spectrum to account for Earth’s rotation, which is significantly faster than the assumed 1-month integration time. To capture Earth’s largest variability, we consider the monthly averages for January (Jan) and July (Jul) from 2017 for each orientation. This yields a total of six different Earth spectra.

Motivated by first LIFE requirement estimates from [Konrad et al. \(2022\)](#) ($R = 50$, $S/N = 10$), we consider two resolving powers ($R = 50, 100$) and two noise levels ($S/N = 10, 20$) for each spectrum. With the LIFE noise model from Section 2.3.3, we determine the wavelength-dependent S/N of the disk-integrated spectra. In Figure 3 we show all six disk-integrated Earth Spectra for the $R = 50$, $S/N = 10$ case.

In Section 3, we compare the retrieved posteriors with ground truth averages for the different views. The ground truths for the P - T profiles and the trace gas abundances of

H₂O, CH₄, and O₃ were derived from the Aqua/AIRS L3 Monthly Standard Physical Retrieval (AIRS-only) 1 degree x 1 degree V7.0 product ([AIRS Project 2020](#)). Ground truth averages for CO₂ were calculated from the OCO-2 GEOS Level 3 monthly dataset (0.5x0.625 assimilated CO₂ V10r at GES DISC; [NASA/GSFC/GMAO Carbon Group 2021](#)), which is derived from observations from the Orbiting Carbon Observatory 2 (OCO-2). We display the ground truths for all views and months in Figure 3. For details on the calculation of these disk-integrated ground truths, we refer to [Mettler et al. \(2024\)](#).

2.3.3. Considered noise models

In the present study, we use two different approaches to model the wavelength-dependent S/N of the considered MIR spectra. First, to test the different forward models on the simulated Earth spectrum, we assume a low-noise scenario. Second, for the retrievals on the disk-integrated Earth spectra, we use a more realistic LIFE-like S/N model. Because the S/N is not constant over the spectrum for both cases, we define the S/N of the spectrum as the S/N in the 11.2 μm wavelength bin (see Figure 4). We choose the 11.2 μm bin since it does not coincide with strong absorption features and thus probes Earth’s continuum emission. This reference wavelength was also used by previous LIFE-related retrieval studies ([Konrad et al. 2022](#); [Alej et al. 2022b](#); [Konrad et al. 2023](#); [Mettler et al. 2024](#); [Alej et al. 2024](#)).

For the low-noise scenario, we only assume photon noise of the source to be present. Thus, if N photons are detected in a given wavelength bin, we assume the noise to be \sqrt{N} . To calculate the S/N , we scale the flux such that the desired S/N is reached at 11.2 μm . The wavelength-dependent photon noise is indicated by the blue-dashed line in Figure 4.

To obtain the more realistic LIFE-like noise estimates, we use the LIFEsim model ([Dannert et al. 2022](#)). In addition to accounting for photon noise of the planet emission, LIFEsim

⁴ We consider monthly averages since this time span roughly corresponds to the expected LIFE integration times specified in [Konrad et al. \(2022\)](#).

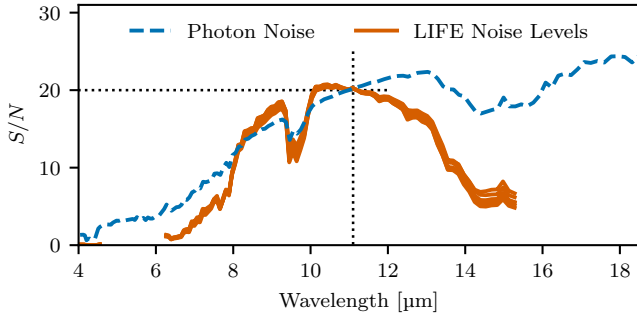


Figure 4. Noise models for the $R = 100$, $S/N = 20$ spectra. The blue-dashed line shows the photon noise assumed for the simulated Earth spectrum. The LIFE_{ESIM} noise assumed for the disk-integrated Earth spectra is shown as solid-red lines. Both noise models reach an S/N of 20 at 11.2 μm (indicated by the black-dotted lines).

models contributions from major astrophysical noise sources (stellar leakage and local- as well as exozodiacal dust emission). Thus, LIFE_{ESIM} makes the implicit assumption that observations with a LIFE-like instrument will not be dominated by instrumental noise terms (Dannert et al., in prep.; Huber et al., in prep.). To calculate the LIFE_{ESIM} noise, we assume the observed planet to orbit a G2V star at 1 AU at a separation of 10 pc from us. The exozodiacal dust emission is set to three times the local zodiacal dust emission, which is the median exozodi emission found for Sun-like stars by the HOSTS survey (Ertel et al. 2020). The wavelength-dependence of the LIFE_{ESIM} noise we assume for the disk-integrated Earth spectra is indicated by the solid-red lines in Figure 4.

For all spectra, we treat the wavelength-dependent S/N as uncertainty on the flux. This implies that the spectral points are set to the true flux values and are not randomized according to the S/N . While randomized spectra provide more accurate simulated observations, retrievals on such noise realizations yield biased parameter posteriors. Ideally, our retrieval study would consider a large number (≥ 10) of different noise realizations of one spectrum. However, such a study is computationally unfeasible due to the large number of required atmospheric retrievals. Alternatively, as motivated in Konrad et al. (2022), retrievals on unrandomized spectra can be used to obtain estimates for the average expected retrieval performance for randomized spectra.

2.4. Prior distributions of model parameters

All prior distributions assumed to run the retrievals are listed in Table 3. We choose the priors for the P - T parameters a_i and the surface pressure P_0 such that the resulting P - T structures cover a wide range of profiles (from cold and thin Mars-like to hot and massive Venus-like atmospheres). For the atmospheric gases N_2 , O_2 , CO_2 , O_3 , and CH_4 , we assume broad uniform priors in log-space that extend from 1 to 10^{-10} in mass fraction. The lower limit of 10^{-10} lies signif-

icantly below the estimated minimal detectable abundances presented in Konrad et al. (2022) ($\approx 10^{-7}$ in mass fraction).

Based on the retrieved abundance constraints from Mettler et al. (2024), we exclude H_2O dominated atmospheres by setting the upper limit of 10^{-1} for the H_2O prior. For planets on Earth-like orbits around G-stars, high H_2O abundances can occur for high partial pressures of CO_2 ($p_{\text{CO}_2} \approx 0.1 - 1$ bar) or other greenhouse gases due to the increased surface temperature (e.g., Wordsworth & Pierrehumbert 2013). Yet, such atmospheres lie close to the critical runaway greenhouse limit and are out of scope for this study. For the $\delta_{\text{H}_2\text{O}}$ parameter, we choose a log-uniform prior between 1 to 10^{-5} . This allows for atmospheric H_2O to deplete by up to five orders of magnitude in the upper atmosphere. Further, the uniform f_C prior between 0 and 1 covers the full range from cloud-free to fully cloudy atmospheres.

We assumed Gaussian priors for the planet radius R_{pl} and mass M_{pl} . The R_{pl} prior is motivated by Dannert et al. (2022), who find that already the detection of a planet with LIFE yields a first R_{pl} estimate. For terrestrial planets in the HZ, they predict a radius estimate R_{est} for the true radius R_{true} of $R_{\text{est}}/R_{\text{true}} = 0.97 \pm 0.18$. We derive the prior for $\log_{10}(M_{\text{pl}})$ from the R_{pl} prior using the statistical mass-radius relation Forecaster (Chen & Kipping 2016). These R_{pl} and M_{pl} priors are in accordance with previous LIFE-related retrieval studies (Konrad et al. 2022, 2023; Alei et al. 2022b; Mettler et al. 2024).

3. RETRIEVAL RESULTS

In the following, we present the results from the validation retrievals on the simulated 1D Earth spectrum in Section 3.1. Thereafter, the findings from the retrievals on the six empirical disk-integrated Earth views are presented in Section 3.2.

3.1. Results for the simulated 1D Earth spectrum

We present the retrieval results for the simulated 1D Earth spectrum (Section 2.3.1) using the three retrieval models $\mathcal{M}_{\text{C,CF}}$, $\mathcal{M}_{\text{V,CF}}$, and $\mathcal{M}_{\text{V,CL}}$ (Table 2, Section 2.2). In Figure 5, we illustrate the constraints retrieved for the P - T structure and the surface conditions. For the $\mathcal{M}_{\text{C,CF}}$ model, the retrieved P - T structure is shifted to lower pressures relative to the ground truth. On average, the surface temperature T_0 is underestimated by 18 K and the surface pressure P_0 by 0.7 dex (‘dex’ reports the value of a quantity q in log-space: $\log_{10}(q) = k$ dex; $q = 10^k \text{Unit}(q)$). With the $\mathcal{M}_{\text{V,CF}}$ model, which accounts for H_2O condensation, these shifts are significantly reduced and the ground truth lies within the 1- σ envelope of the retrieved P - T structure. Yet, P_0 remains slightly underestimated ($\log_{10}(P_0) = 0.3 \pm 0.2$ dex) and the T_0 constraint is not improved. The $\mathcal{M}_{\text{V,CL}}$ model, which assumes a partial cloud coverage, yields the most accurate constraints for the P - T structure. The true P_0 lies within the 16%-84%

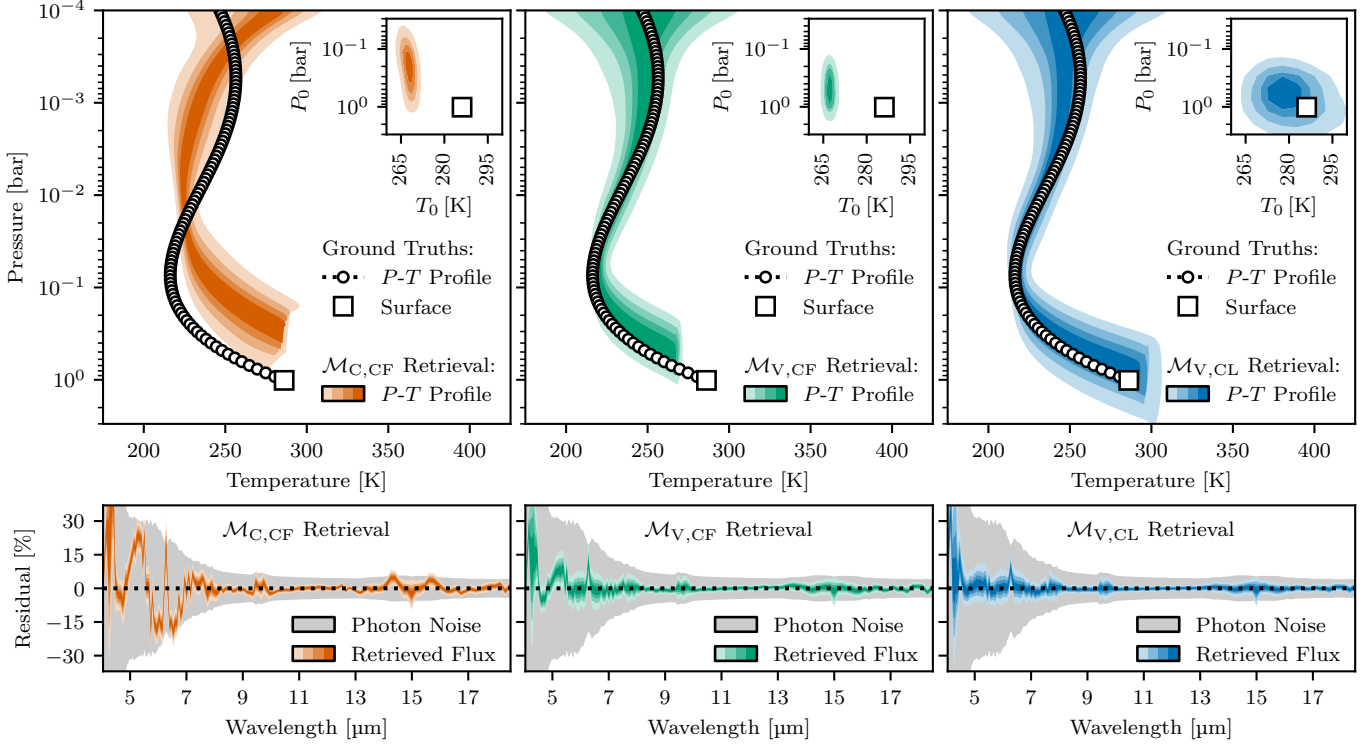


Figure 5. P - T fits (top row) and flux residuals (bottom row) for the retrievals on the simulated $R = 100$, $S/N = 20$ Earth spectrum. Each column provides the results for a different retrieval model (from left to right: $\mathcal{M}_{C,CF}$, $\mathcal{M}_{V,CF}$, and $\mathcal{M}_{V,CL}$). Color-shaded areas indicate retrieval percentiles (from light to dark colors: 5 – 95%, 15 – 85%, 25 – 75%, and 35 – 65%). In the P - T figures, white squares mark the true surface conditions (P_0 , T_0) and white circles the true P - T structure. The inlay in the top right of the P - T panel shows the retrieved constraints on the surface conditions. In the flux residual figures, the gray-shaded area indicates the assumed $1\text{-}\sigma$ photon noise level.

percentile range of the posterior ($\log_{10}(P_0) = 0.2 \pm 0.3$ dex). The estimate for T_0 is also improved significantly, but the uncertainty is increased ($T_0 = 280 \pm 8$ K).

The flux residuals in Figure 5 show that the $\mathcal{M}_{C,CF}$ model fails to accurately fit the input spectrum. Especially in the strong absorption features of H_2O ($4.5 - 7.5 \mu\text{m}$), O_3 ($9 - 10 \mu\text{m}$), and CO_2 ($14 - 16 \mu\text{m}$), the fitted flux differs significantly from the input, which indicates these features cannot be modeled correctly. In contrast, the $\mathcal{M}_{V,CF}$ retrieval provides an accurate fit to the input spectrum above $\sim 5.5 \mu\text{m}$, which is in agreement with the improvements observed for the P - T structure. Finally, the $\mathcal{M}_{V,CL}$ model yields further minor improvements over the $\mathcal{M}_{V,CF}$ model in the high noise regime of the input spectrum between $4 - 6 \mu\text{m}$.

In Figure 6 and Table 5, we summarize the retrieved posteriors for the forward model parameters. We provide the posteriors for the surface conditions, the planet radius R_{pl} , the atmospheric trace gases, the drying parameter $\delta_{\text{H}_2\text{O}}$, and the cloud fraction f_C . The a_i posteriors are visualized by the retrieved P - T structures in Figure 5. The posteriors for M_{pl} , N_2 , and O_2 are not shown, since they were not constrained over the assumed priors. Last, we derived estimates for the planet’s equilibrium temperature T_{eq} and Bond albedo A_B from the posteriors. For T_{eq} , we calculated the MIR spec-

tra corresponding to the points in the posterior and integrated these spectra to obtain the total MIR emission. We then defined T_{eq} as the temperature of a spherical black-body with radius R_{pl} that emits the same total flux. From T_{eq} , we then determined A_B :

$$A_B = 1 - 16\pi\sigma \frac{a_P^2 T_{\text{eq}}^4}{L_*}. \quad (8)$$

Here, a_P is the exoplanet’s semi-major axis and L_* the star’s luminosity. For details on the derivation of T_{eq} and A_B , we refer to [Mettler et al. \(2024\)](#).

As seen for the P - T structures, both the P_0 and T_0 posteriors are biased relative to the ground truth for the $\mathcal{M}_{C,CF}$ retrieval. Due to a degeneracy between the pressure-induced line-broadening and the abundances of the atmospheric trace-gases (see, e.g., [Misra et al. 2014](#); [Schwieterman et al. 2015](#); [Alej et al. 2022a](#)), we expect the underestimation of the pressures to be accompanied by an overestimation of the trace-gas abundances. Indeed, the CO_2 , O_3 , and CH_4 abundances are overestimated by 0.9 dex to 1.4 dex by the $\mathcal{M}_{C,CF}$ retrieval. For the $\mathcal{M}_{V,CF}$ and $\mathcal{M}_{V,CL}$ retrievals, which yield better pressure constraints, the abundance estimates are unbiased (i.e., the ground truths fall within the 16%-84% posterior range). Only the H_2O abundance, which decreases

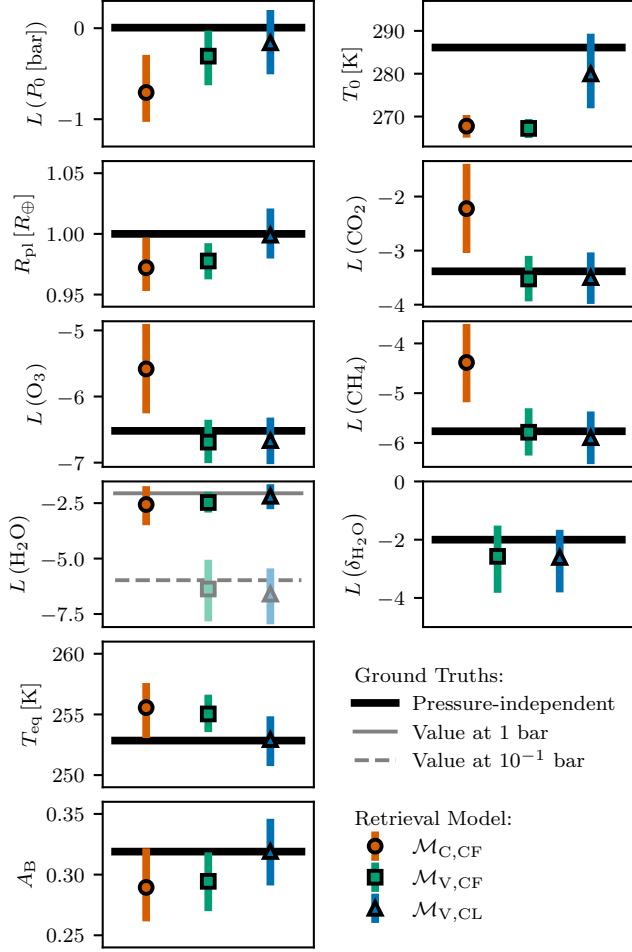


Figure 6. Posteriors from retrievals on the simulated $R = 100$, $S/N = 20$ Earth spectrum. Here, $L(\cdot)$ stands for $\log_{10}(\cdot)$. Thick black lines indicate pressure-independent ground truths. Thin gray lines show the true H_2O abundance at 1 bar (solid line) and at 10^{-1} bar (dashed line). The different markers represent the retrieval models: orange circles – $\mathcal{M}_{\text{C,CF}}$, green squares – $\mathcal{M}_{\text{V,CF}}$, and blue triangles – $\mathcal{M}_{\text{V,CL}}$. The colored lines indicate the 16% – 84% posterior percentiles. For the $\mathcal{M}_{\text{V,CF}}$ and $\mathcal{M}_{\text{V,CL}}$ models, which assume variable H_2O profiles, we provide both the retrieved H_2O abundance at P_0 (dark marker color) and at 1 dex below P_0 (light marker color).

strongly with altitude in Earth’s atmosphere, is not overestimated by the $\mathcal{M}_{\text{C,CF}}$ retrieval. The retrieved abundance lies between the 1 bar and 10^{-1} bar ground truth, roughly 0.5 dex below the surface abundance (see Table 5). For the $\mathcal{M}_{\text{V,CF}}$ retrieval, the abundance at 10^{-1} bar is accurately estimated. Yet, since P_0 and T_0 are underestimated, the condensation model underestimates the surface H_2O abundance by 0.4 dex. With the $\mathcal{M}_{\text{V,CL}}$ model, this bias on the surface abundance of H_2O is removed. The $\delta_{\text{H}_2\text{O}}$ estimates from the $\mathcal{M}_{\text{V,CF}}$ and $\mathcal{M}_{\text{V,CL}}$ scenarios do not differ significantly. In both cases, values of $\delta_{\text{H}_2\text{O}} > 10^{-1}$ are ruled out. Thus, an Earth-like H_2O depletion in the upper atmosphere is in principle detectable from the MIR thermal emission.

Table 5. Numeric values for the posteriors in Figure 6.

Parameter	Ground Truths	Posteriors		
		$\mathcal{M}_{\text{C,CF}}$	$\mathcal{M}_{\text{V,CF}}$	$\mathcal{M}_{\text{V,CL}}$
$L(P_0)$ [bar]	0.0	$-0.7^{+0.4}_{-0.3}$	$-0.3^{+0.2}_{-0.3}$	$-0.2^{+0.3}_{-0.3}$
T_0 [K]	286	268^{+2}_{-2}	267^{+1}_{-1}	280^{+8}_{-7}
R_{pl} [R_{\oplus}]	1.00	$0.97^{+0.02}_{-0.02}$	$0.98^{+0.01}_{-0.01}$	$1.00^{+0.02}_{-0.02}$
$L(\text{CO}_2)$	-3.4	$-2.2^{+0.8}_{-0.7}$	$-3.5^{+0.4}_{-0.3}$	$-3.5^{+0.4}_{-0.4}$
$L(\text{O}_3)$	-6.5	$-5.6^{+0.6}_{-0.6}$	$-6.7^{+0.3}_{-0.3}$	$-6.7^{+0.3}_{-0.3}$
$L(\text{CH}_4)$	-5.8	$-4.4^{+0.7}_{-0.7}$	$-5.8^{+0.4}_{-0.4}$	$-5.9^{+0.5}_{-0.5}$
$L(\text{H}_2\text{O})$	-2.1	$-2.6^{+0.7}_{-0.8}$	$-2.5^{+0.3}_{-0.3}$	$-2.2^{+0.4}_{-0.4}$
$L(\delta_{\text{H}_2\text{O}})$	-2.0	...	$-2.6^{+0.9}_{-1.1}$	$-2.6^{+0.8}_{-1.1}$
f_{C}	0.67	$0.54^{+0.17}_{-0.21}$
T_{eq} [K]	253	256^{+2}_{-2}	255^{+1}_{-1}	253^{+2}_{-2}
A_{B}	0.32	$0.29^{+0.03}_{-0.02}$	$0.29^{+0.02}_{-0.02}$	$0.32^{+0.02}_{-0.02}$

NOTE—Here, $L(\cdot)$ stands for $\log_{10}(\cdot)$. The second column lists the assumed ground truths (see Table 3 for details). In the last three columns, we list the median and the 16%–84% range (via \pm indices) of the parameter posteriors for the $\mathcal{M}_{\text{C,CF}}$, $\mathcal{M}_{\text{V,CF}}$, and $\mathcal{M}_{\text{V,CL}}$ models. For H_2O , all listed values correspond to the surface-layer abundances.

Similar to T_0 , R_{pl} is underestimated by $\sim 0.03 R_{\oplus}$ by the $\mathcal{M}_{\text{C,CF}}$ and $\mathcal{M}_{\text{V,CF}}$ retrievals. This bias is propagated to the T_{eq} and A_{B} estimates, since they are derived from the R_{pl} posterior. For the $\mathcal{M}_{\text{C,CF}}$ and $\mathcal{M}_{\text{V,CF}}$ retrievals, the underestimated R_{pl} translates to an overestimated T_{eq} (by ~ 3 K) and an underestimated A_{B} (by ~ 0.03). Thus, a too small R_{pl} is compensated with an increased T_{eq} , which requires a lower A_{B} . In contrast, the retrievals using the true $\mathcal{M}_{\text{V,CL}}$ model yield accurate and bias-free estimates for R_{pl} , T_{eq} , and A_{B} .

Last, in the $\mathcal{M}_{\text{V,CL}}$ retrievals, we aim to constrain the cloud fraction f_{C} . We show the f_{C} , R_{pl} , and T_0 posteriors from the $\mathcal{M}_{\text{V,CL}}$ retrieval in the corner plot in Figure 7. While f_{C} is not strongly constrained over the prior range, we observe significant correlations between f_{C} and the other parameters. The correlation between f_{C} and T_0 implies that a higher T_0 can be compensated with a higher f_{C} , since atmospheric clouds block the thermal emission from the warm near-surface layers. This degeneracy explains the observed increase in the T_0 uncertainty for the $\mathcal{M}_{\text{V,CL}}$ retrieval. Further, f_{C} is weakly correlated with R_{pl} (higher f_{C} lead to higher R_{pl}), which explains why R_{pl} estimates are improved for the $\mathcal{M}_{\text{V,CL}}$ model.

Finally, we use Bayes’ factor K (values in Table A1) to benchmark the models against each other. We find that $\mathcal{M}_{\text{V,CF}}$ is preferred over $\mathcal{M}_{\text{C,CF}}$ ($|\log_{10}(K)| = 3.7 \pm 0.1$), and $\mathcal{M}_{\text{V,CL}}$ outperforms $\mathcal{M}_{\text{C,CF}}$ ($|\log_{10}(K)| = 4.3 \pm 0.1$). Thus, an accurate model for Earth’s H_2O abundance profile is required to correctly fit its MIR spectrum. This agrees with our

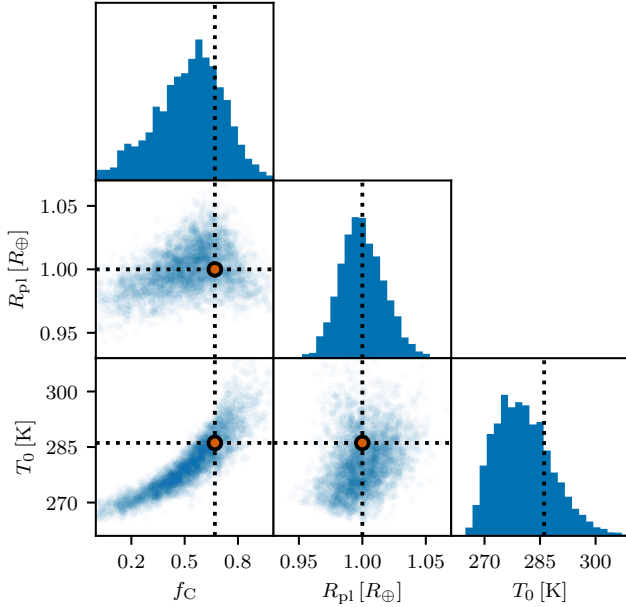


Figure 7. Corner plot for the f_c , R_{pl} , and T_0 posteriors (in blue) for the retrieval with the $\mathcal{M}_{V,CL}$ forward model on the simulated $R = 100$, $S/N = 20$ Earth spectrum. The black-dashed lines and the circular orange markers indicate the parameter ground truths.

findings for the retrieved P – T structures, flux residuals, and parameter posteriors. Further, $\mathcal{M}_{V,CL}$ is slightly preferred over the cloud-free $\mathcal{M}_{V,CF}$ model ($|\log_{10}(K)| = 0.6 \pm 0.1$). This slight preference agrees with the small improvements observed for the flux residuals. Yet, despite the limited improvements in the spectral fit, the degeneracies associated with f_c help improve the estimates for T_0 , R_{pl} , T_{eq} , and A_B .

3.2. Results for real disk-integrated Earth spectra

Here, we present the retrieval results for the empirical disk-integrated Earth views (Section 2.3.2) for the $\mathcal{M}_{C,CF}$, $\mathcal{M}_{V,CF}$, and $\mathcal{M}_{V,CL}$ retrieval models (Table 2, Section 2.2). In Figure 8, we show the retrieved P – T structures for the $R = 100$, $S/N = 10$ EqC Jul Earth spectrum. Further, we show the residuals of the fitted spectra relative to the input spectrum. The P – T results and the residuals for all other views, R , and S/N scenarios are comparable and thus not shown.

The P – T structures retrieved for the $\mathcal{M}_{C,CF}$ model exhibit similar characteristics as the results for the simulated spectrum. The retrieved constraints are systematically shifted toward lower pressures. Also P_0 is underestimated by 0.4 dex to 0.6 dex depending on the view. In contrast, T_0 is well approximated by the $\mathcal{M}_{C,CF}$ retrievals (truths lie in the 16% – 84% posterior range). While shifts in the retrieved P – T profiles relative to the ground truth are also observed for $\mathcal{M}_{V,CF}$, the $\mathcal{M}_{V,CL}$ runs yield accurate constraints. However, for both $\mathcal{M}_{V,CF}$ and $\mathcal{M}_{V,CL}$, the P – T constraints, which extend significantly beyond the true P_0 and T_0 , indicate that the sur-

face conditions are no longer well constrained. This suggests that the high-pressure layers of the fitted model atmosphere do not contribute significantly to the MIR thermal emission emerging at the top of the atmosphere. Alternatively, we can consider the pressure ($P_{Op.}$) and temperature ($T_{Op.}$) in the deepest layer in the model atmosphere that still contributes to the simulated MIR spectrum. Thus, $P_{Op.}$ and $T_{Op.}$ correspond to the pressure and temperature at which the simulated atmosphere becomes opaque in the MIR. For an optically thin atmosphere, we simply obtain: $P_{Op.} = P_0$ and $T_{Op.} = T_0$. We observe that $P_{Op.}$ and $T_{Op.}$ roughly correspond to the ground truths for P_0 and T_0 . Thus, the fitted model atmospheres become opaque close to Earth’s true surface.

The flux residuals in Figure 8 do not differ significantly between the models. Around the $7.7 \mu\text{m}$ N_2O band, the models struggle to fit the spectrum accurately, since they do not include N_2O . Mettler et al. (2024) showed that, for the empirical disk-integrated Earth spectra we consider here, models including N_2O are not preferred by Bayesian model selection. At all other wavelengths, the three models provide an accurate fit. This observation is supported by model comparison via the Bayes factor K (values in Table A1). For all $R = 50$ and most $R = 100$ spectra, no model is preferred over the others ($|\log_{10}(K)| \leq 0.3$; uncertainty ± 0.2). Rare exceptions occur for the $R = 100$, $S/N = 20$ spectra, where slight preferences for $\mathcal{M}_{V,CF}$ or $\mathcal{M}_{V,CL}$ are occasionally observed ($|\log_{10}(K)| \leq 0.6$; uncertainty ± 0.2).

In Figure 9, we visualize the posteriors retrieved with the $\mathcal{M}_{C,CF}$, $\mathcal{M}_{V,CF}$, and $\mathcal{M}_{V,CL}$ models for the EqC Jul view at a LIFESIM S/N of 10. The results for the other views and the $S/N = 20$ retrievals exhibit the same general behavior and are provided in Figures A1 and A2 in Appendix A. Further, the numeric values for all posteriors are listed in Tables A2, A3, and A4. We show the posteriors for P_0 , T_0 , $P_{Op.}$, $T_{Op.}$, R_{pl} , the trace-gas abundances, $\delta_{\text{H}_2\text{O}}$, and f_c . The a_i posteriors are visualized via the P – T constraints in Figure 8. We do not show the M_{pl} , N_2 , and O_2 posteriors, since they are not constrained over the assumed priors. The T_{eq} and A_B estimates were derived from the posteriors (see Section 3.1).

We observe that the posteriors for the different models exhibit trends similar to the ones observed for the simulated 1D Earth spectra in Section 3.1. For the $\mathcal{M}_{C,CF}$ model, the underestimated P_0 values are accompanied by overestimated abundances of CO_2 (by ≥ 0.6 dex) and CH_4 (by ≥ 1.0 dex). For O_3 , the pressure-dependent ground truths cover a wide range of abundances. Thus, the pressure-induced biases are not directly observable. Next, the $\mathcal{M}_{C,CF}$ posteriors for H_2O underestimate the true surface-layer abundances by 0.5 dex to 1.0 dex. Further, R_{pl} is consistently underestimated by $\geq 0.05 R_{\oplus}$, which translates to biases for the derived parameters T_{eq} and A_B (T_{eq} overestimated by ≥ 5 K; A_B underes-

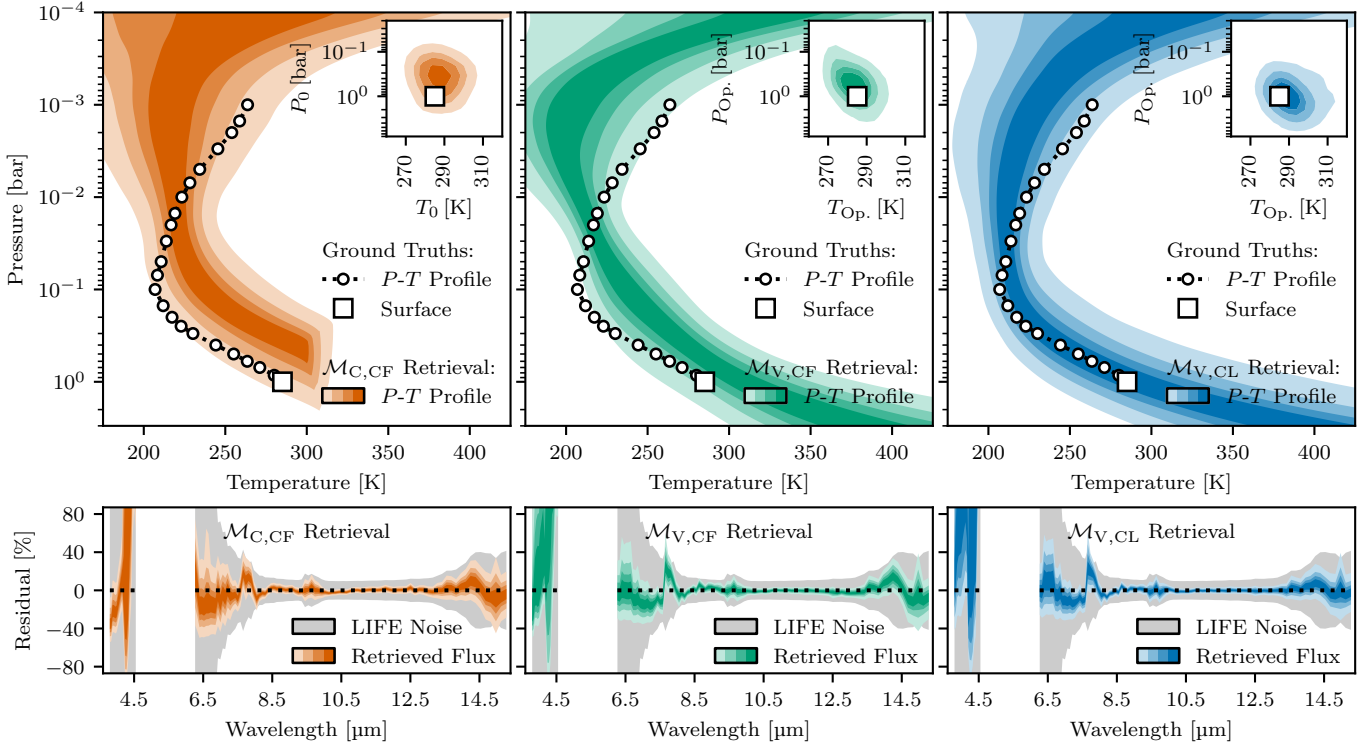


Figure 8. P - T fits (top row) and flux residuals (bottom row) for the retrievals on the $R = 100$, $S/N = 10$ EqC Jul spectrum of Earth. Each column provides the results for a different retrieval model (from left to right: $\mathcal{M}_{C,CF}$, $\mathcal{M}_{V,CF}$, and $\mathcal{M}_{V,CL}$). Color-shaded areas indicate retrieval percentiles (from light to dark colors: 5 – 95%, 15 – 85%, 25 – 75%, and 35 – 65%). In the P - T figures, white squares mark the true surface conditions (P_0 , T_0) and white circles the true P - T structure. The inlay in the top right of the P - T panel shows the retrieved constraints on the surface conditions (P_0 , T_0) for the $\mathcal{M}_{C,CF}$ case. For the $\mathcal{M}_{V,CF}$ and $\mathcal{M}_{V,CL}$ scenario, the inlay shows the pressure and temperature where the atmosphere becomes opaque (P_{Op} , T_{Op}). In the flux residual figures, the gray-shaded area indicates the assumed 1 - σ LIFESM-noise level.

timed by ≥ 0.05). Only T_0 is accurately estimated by T_{Op} for most scenarios.

For $\mathcal{M}_{V,CF}$ and $\mathcal{M}_{V,CL}$, significant improvements in the parameter estimates are observable. Generally, the P_0 estimates are higher than for the $\mathcal{M}_{C,CF}$ runs. As seen with the P - T profiles, several $\mathcal{M}_{V,CF}$ and $\mathcal{M}_{V,CL}$ retrievals only yield lower limits for P_0 and T_0 . In these cases, the P_{Op} value indicates that the high-pressure layers of the model atmosphere do not contribute to the MIR spectrum and thus P_0 and T_0 cannot be constrained further. The retrieved P_{Op} estimates increase with the model complexity and mostly coincide with the P_0 ground truth for the $\mathcal{M}_{V,CL}$ retrievals. Further, T_{Op} provides accurate estimates for T_0 in the $\mathcal{M}_{V,CF}$ retrievals. For $\mathcal{M}_{V,CL}$, T_{Op} generally overestimates T_0 and the uncertainties are often significantly increased. This is due to the aforementioned degeneracy between f_C and T_0 , where too high T_0 can be compensated by a higher f_C . Also, the retrieved estimates for R_{pl} and the derived parameters T_{eq} and A_B are significantly improved, especially for the $\mathcal{M}_{V,CL}$ retrievals.

For the trace-gas abundances, the biases observed for the $\mathcal{M}_{C,CF}$ retrievals are continually reduced as we include H_2O condensation and clouds. The $\mathcal{M}_{V,CL}$ model yields the best estimates for the atmospheric CO_2 abundances. For all

$\mathcal{M}_{V,CL}$ cases considered, the CO_2 ground truths lie in the 16% – 84% percentile range of the posteriors. Also for CH_4 , the biases are reduced and the $\mathcal{M}_{V,CL}$ posteriors estimate the ground truths accurately for most scenarios. Yet, for some $R = 50$, $S/N = 10$ scenarios, CH_4 is no longer detectable. In these cases, only an upper limit is obtained for the CH_4 abundance ($\approx -6.0 \pm 0.2$ dex). For O_3 , we observe a significant reduction in the retrieved abundance. This indicates that the O_3 estimate in the $\mathcal{M}_{C,CF}$ retrieval is affected by the same pressure-abundance degeneracy as CO_2 and CH_4 . Last, the H_2O abundance at P_{Op} provides accurate estimates for Earth’s ground truth surface abundance of H_2O . Further, the structure of the H_2O profile is accurately approximated by both the $\mathcal{M}_{V,CF}$ and $\mathcal{M}_{V,CL}$ retrievals.

Lastly, all retrievals yield similar constraints for δ_{H_2O} and f_C independent of the disk-integrated Earth spectrum considered. As for the simulated Earth spectrum in Section 3.1, only high values of $\delta_{H_2O} > 10^{-1}$ can be ruled out for both the $\mathcal{M}_{V,CF}$ and the $\mathcal{M}_{V,CL}$ model. Further, the $\mathcal{M}_{V,CL}$ retrievals often struggle to constrain f_C due to the aforementioned correlations with T_{Op} . Generally, values of $f_C \approx 0.5 \pm 0.2$ are retrieved and only f_C lower than 0.1 can be ruled out confi-

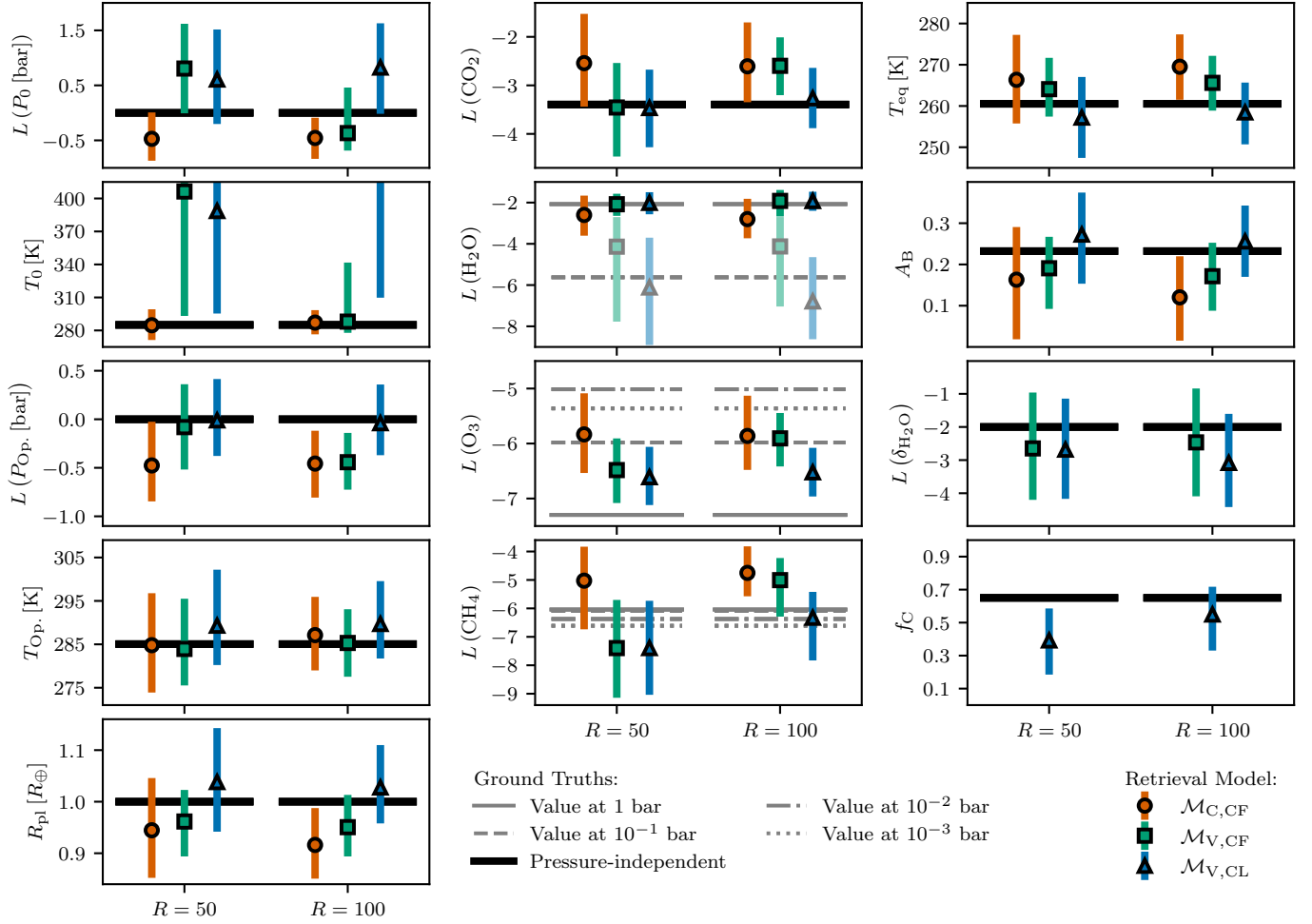


Figure 9. Posteriors from the retrievals on the EqC Jul spectra of Earth (LIFE_{SIM} $S/N = 10$; $R = 50, 100$). Here, $L(\cdot)$ stands for $\log_{10}(\cdot)$. Thick black lines indicate pressure-independent ground truths. Thin gray lines show the ground truth abundances at different atmospheric pressures (solid: 1 bar; dashed: 10^{-1} bar; dashed-dotted: 10^{-2} bar; dotted: 10^{-3} bar). The markers represent the retrieval models: orange circles – $\mathcal{M}_{C,CF}$, green squares – $\mathcal{M}_{V,CF}$, and blue triangles – $\mathcal{M}_{V,CL}$. The colored lines indicate the 16% – 84% posterior percentiles. For the $\mathcal{M}_{V,CF}$ and $\mathcal{M}_{V,CL}$ models, which assume variable H_2O profiles, we provide both the retrieved H_2O abundance at the pressure P_{Op} , where the atmosphere becomes optically thick (dark marker color) and at 1 dex below P_{Op} (light marker color).

dently. In some $S/N = 20$ retrievals, the lower limit obtained for f_c is significantly higher (lower limit on f_c : ≈ 0.5).

4. DISCUSSION

Here, we outline implications of our work for the characterization of terrestrial HZ exoplanets (Section 4.1) and for the LIFE mission requirements (Section 4.2). Thereafter, in Section 4.3, we point out the limitations of the present study.

4.1. Implications for Characterizing Rocky HZ Exoplanets

We find that the biased estimates for the P – T structure and the atmospheric composition obtained in the $\mathcal{M}_{C,CF}$ retrievals are predominantly attributable to two simplifying assumptions commonly made by retrieval models: vertically constant abundance profiles and a cloud-free atmosphere. Our results for the $\mathcal{M}_{V,CF}$ and $\mathcal{M}_{V,CL}$ retrieval models demonstrate that including physically motivated models for Earth’s

atmospheric H_2O profile and partial cloud coverage helps significantly improve the accuracy of the retrieved parameter estimates. However, despite the improved parameter estimates, neither the $\mathcal{M}_{V,CF}$ nor the $\mathcal{M}_{V,CL}$ model is preferred over the $\mathcal{M}_{C,CF}$ model by Bayesian model comparison for LIFE-like R and S/N scenarios. Yet, we argue that the usage of the $\mathcal{M}_{V,CF}$ and $\mathcal{M}_{V,CL}$ models is justifiable, since both impose physics informed constraints on the model atmosphere. This allows to exclude unrealistic atmospheric states and thereby yields more reliable parameter estimates. Especially for HZ exoplanets, unbiased parameter constraints are a critical requirement to enable the accurate assessment of their habitability. Further, in the same context, biased estimates for the abundances of potential biosignature gases, such as CH_4 , can be highly problematic.

From Figure 3 and Mettler et al. (2023), we know that Earth’s MIR emission spectrum depends significantly on both the observed view and the season. Since both the viewing geometry and the season will be unknown for future observations of HZ terrestrial exoplanets, it is crucial to understand if and how these factors affect our characterization. We find that, independent of the assumed retrieval model, the retrieved constraints for most of the model parameters exhibit no significant dependence on the view and season of the Earth spectrum. Only T_0 , T_{Op} , T_{eq} , and A_B exhibit a perceptible dependence on the considered spectrum in the high R and S/N scenarios (see Figures A1 and A2). These findings are in agreement with Mettler et al. (2024), who performed retrievals on the same set of disk-integrated Earth spectra considered here using the $\mathcal{M}_{\text{C,CF}}$ forward model.

4.2. Implications for the LIFE Initiative

Several retrieval studies have evaluated how well rocky HZ exoplanets could be characterized from their MIR spectrum by a LIFE-like observatory. In Konrad et al. (2022), preliminary minimal requirements for LIFE are obtained by analyzing simulated Earth spectra. By requiring a detection of the potential biosignature CH_4 with LIFE, the authors find lower limits of 4 – 18.5 μm for the wavelength coverage, 50 for R , and 10 for S/N . In two follow-up studies (Alei et al. 2022b; Konrad et al. 2023), these findings are reevaluated on simulated spectra of Earth at different temporal epochs from Rugheimer & Kaltenegger (2018) and a cloudy Venus-like planet. Last, Mettler et al. (2024) test the LIFE requirements on the same real disk- and time-averaged MIR Earth spectra we considered here.

While the analyzed spectra vary significantly in complexity, all previous studies assumed retrieval models with vertically constant abundance profiles. Further, only Konrad et al. (2023) accounted for clouds in their retrieval models. All studies yield similar results for the strengths of the parameter constraints and the detectability of trace-gases. They find Earth-like levels of H_2O , CO_2 , O_3 , and CH_4 to be detectable. Further, the retrieved 16% – 84% posterior range does not exceed ± 0.5 dex for pressures, ± 20 K for temperatures, $\pm 0.1 R_{\oplus}$ for R_{pl} , and ± 1.0 dex for trace-gas abundances. These constraints from the previous LIFE studies are consistent with our results for the $\mathcal{M}_{\text{C,CF}}$ retrieval model, which also assumes constant abundance profiles and neglects clouds.

However, similar to our findings for $\mathcal{M}_{\text{C,CF}}$ retrievals, both Alei et al. (2022b) and Mettler et al. (2024) observe significant biases in the retrieved posteriors relative to the ground truths. Both studies analyzed spectra of cloudy atmospheres with non-constant trace-gas abundances. Mettler et al. (2024) argue that underestimated pressures and overestimated trace-gas abundances are primarily evoked by the retrieval model assumption of a vertically constant H_2O profile. In contrast,

biased temperature, R_{pl} , and A_B estimates are attributable primarily to neglecting clouds. Our findings for the simulated Earth spectrum (Section 3.1) validate these claims. In the $\mathcal{M}_{\text{V,CF}}$ retrievals, biases on pressure and abundance estimates are reduced significantly by modeling Earth’s H_2O abundance profile. Yet, temperature, R_{pl} , and A_B estimates are largely unaffected. These biases are only reduced in the cloudy $\mathcal{M}_{\text{V,CL}}$ retrievals. Also our findings for the real disk-integrated Earth views (Section 3.2) validate the claims from Mettler et al. (2024) by exhibiting similar bias reductions. However, the improved estimates for individual parameters are no longer attributable to solely the variable H_2O profile or the inclusion of clouds.

We observe two additional important differences between the $\mathcal{M}_{\text{V,CF}}$ and $\mathcal{M}_{\text{V,CL}}$ retrieval results and the previous studies. First, we do not retrieve accurate estimates for P_0 and T_0 for most views independent of the R and S/N of the spectrum. The retrieved H_2O profiles indicate that the H_2O abundance in the lower atmosphere is increased by ≥ 0.5 dex compared to the $\mathcal{M}_{\text{C,CF}}$ model. These elevated H_2O levels lead to an optically thick lower atmosphere due to the strong MIR continuum opacity of H_2O . As a result, the high-pressure layers of the model atmosphere do not contribute to the exoplanet’s MIR spectrum and therefore only lower limits for P_0 and T_0 are attainable. The pressure P_{Op} of the lowest atmosphere layer that still contributes to the modelled MIR spectrum roughly corresponds to the ground truth P_0 value. Thus, the model atmosphere becomes opaque to MIR radiation close to Earth’s surface. This agrees well with measurements of the MIR opacity of Earth’s atmosphere (see, e.g., Harries et al. 2008). This finding can be generalized to exoplanets, where clouds and the MIR opacity sources set a fundamental limit on how deep an atmosphere can be probed.

Second, at the minimal R and S/N requirements from Konrad et al. (2022) ($R = 50$, $S/N = 10$), Earth-like CH_4 mass fractions of 10^{-6} are not reliably detected in the $\mathcal{M}_{\text{V,CF}}$ and $\mathcal{M}_{\text{V,CL}}$ retrievals. Instead, most of these retrieval runs yield upper limits of $\log_{10}(\text{CH}_4) \leq 5.0 \pm 0.5$ dex for the CH_4 abundance. This occurs since Earth’s main MIR CH_4 signature at ~ 8 μm overlaps with a strong H_2O band (5 – 8 μm). Thus, changes to the H_2O abundance model directly impact the CH_4 retrieval. Importantly, the main driver for the initial R and S/N requirements was the capability to detect CH_4 in an Earth-like atmosphere. Our results indicate that a bias-free constraint on the CH_4 abundance (mean of CH_4 posterior within 0.5 dex of 1 bar ground truth; uncertainty $\leq \pm 1.0$ dex) at $R = 50$ is only possible for $S/N \geq 20$. For the $R = 100$ scenarios, such CH_4 constraints remain possible for $S/N = 10$.

Last, while the simulation-based LIFE studies analyzed the MIR emission between 4–18.5 μm , the empirical Earth spectra studied here and in Mettler et al. (2024) cover a smaller range (3.75 – 4.6 μm , 6.2 – 15.4 μm). Yet, the constraints

we retrieved for the $\mathcal{M}_{C,CF}$ model are comparable to the previous studies. This suggests that measurements of the MIR flux above $15.4\ \mu\text{m}$ and between $4.6 - 6.2\ \mu\text{m}$ are not essential to accurately characterize an exo-Earth with LIFE. However, additional studies are required to investigate whether this finding generalizes to arbitrary HZ terrestrial exoplanets.

4.3. Limitations and Future Work

The present study demonstrates, that adding simple physical constraints to the retrieval forward model can help significantly reduce biases in the retrieved posteriors for an Earth-like spectrum. Yet, there are limitations inherent to our work, the effect of which must be investigated in future studies.

First, our model for the atmospheric H_2O profile assumed that condensation occurs if the relative humidity reaches 100%. Thus, physical tropospheric states, such as the H_2O supersaturation of air (e.g., Spichtinger et al. 2003; Genthon et al. 2017), are not possible. Yet, since we are only sensitive to order of magnitude changes in the H_2O abundance for the R and S/N scenarios considered, we do not expect such factors to significantly affect our findings. Further, we assumed that only condensation affects the H_2O profile. However, in the stratosphere and above, the H_2O abundance is strongly affected by additional processes such as the photochemical oxidation of CH_4 (e.g., Jones et al. 1986; Frank et al. 2018). Yet, since the bulk of Earth’s MIR emission originates from the troposphere, we argue that the stratospheric H_2O profile only affects our characterization negligibly.

Second, we assume constant abundance profiles for all trace-gases except for H_2O . On Earth, especially the O_3 but also the CH_4 abundances exhibit significant altitude dependencies (see Figure 3). These variations are predominantly evoked by photochemical processes in the stratosphere (Chapman 1932; Jones et al. 1986). However, in contrast to H_2O , a simple physical constraint for the O_3 and CH_4 profiles does not exist (e.g., Kozakis et al. 2022). As a result, models for these profiles would be relatively unconstrained. In addition, the MIR spectral feature of O_3 at $9.7\ \mu\text{m}$ originates from the high pressure layers in Earth’s atmosphere ($p > 0.3\ \text{bar}$). Consequentially, we are not sensitive to the large O_3 variations in the upper atmosphere at the considered R and S/N . Also for CH_4 , the main contribution to the MIR feature at $7.7\ \mu\text{m}$ originates from the high pressure layers ($p > 10^{-1}\ \text{bar}$). The vertical variations in the ground truths in these layers ($\pm 0.1\ \text{dex}$) are significantly smaller than the uncertainties on the CH_4 posteriors ($\geq \pm 0.5\ \text{dex}$). Given the limited spectral information available, the impact of the O_3 and CH_4 variations on our results is likely negligible.

Third, instead of modelling the wavelength-dependent MIR opacity of H_2O clouds, we assume gray clouds. Further, we assume the clouds to form in a single atmosphere layer. In contrast, for Earth, the position of the cloud-top is variable

(p_C ranges from $\sim 0.1 - 0.9\ \text{bar}$; e.g., Kokhanovsky et al. 2011). However, the MIR optical properties of clouds do not vary strongly with wavelength or pressure (Petty 2006). Furthermore, findings presented in Konrad et al. (2023) suggest that physical cloud properties (such as cloud composition and particle size) cannot be constrained for the LIFE R and S/N scenarios considered here. Thus, given the limited information content of the spectra studied, the assumption of gray clouds at a fixed height is justifiable.

Fourth, we parameterized the atmospheric $P-T$ profile using a fourth order polynomial. This model has the benefit of being highly flexible. Since it does not impose any physical constraints, it can fit any $P-T$ structure. However, limiting the atmospheric $P-T$ structure to physically viable states by using a learning-based parametrization (see, e.g. Gebhard et al. 2023) could help improve our characterization. This is especially promising for the $\mathcal{M}_{V,CF}$ and $\mathcal{M}_{V,CL}$ models, since they link the H_2O abundance profile and the clouds to the atmospheric $P-T$ structure. However, for terrestrial atmospheres, the reliability of learning-based $P-T$ models is currently limited by the availability of sufficient training data.

Fifth, we focus on Earth’s MIR emission spectrum, which provides an excellent benchmark (e.g., Robinson & Salvador 2023). Our finding that neglecting vertical abundance variations and clouds affects the retrieved parameter estimates can be generalized to terrestrial exoplanets. Yet, rocky exoplanets will exhibit atmospheres different from Earth. Thus, detailed studies similar to what Rowland et al. (2023) did for cloudy L-dwarfs are required for terrestrial exoplanets to search for additional model assumptions that could affect the interpretation of MIR thermal emission spectra.

Last, the comparison of different retrieval approaches has revealed that the obtained parameter posteriors can depend on framework particularities such as the radiative transfer implementation, the parameter sampling algorithm, or the used molecular line opacities (e.g., Line et al. 2013; Barstow et al. 2020; Alei et al. 2022a). Community efforts (e.g., the CUISINES Working Group⁵) that aim to benchmark, compare, and validate different retrieval frameworks on real and simulated spectral data are indispensable to ensure the correct characterization of HZ terrestrial exoplanet atmospheres in the future.

5. SUMMARY AND CONCLUSIONS

In this study, we investigated how common atmospheric retrieval assumptions can bias the characterization of terrestrial HZ exoplanets. Specifically, we tested how model assumptions for the vertical H_2O abundance profile and the atmospheric clouds impact our characterization of Earth as an exoplanet by running retrievals with different forward mod-

⁵ <https://nexss.info/cuisines/>

els. The baseline model ($\mathcal{M}_{C,CF}$) assumed a cloud-free atmosphere with constant abundance profiles for all trace-gases. While still cloud-free, the $\mathcal{M}_{V,CF}$ model estimated the H_2O abundance profile by accounting for H_2O condensation. Last, the $\mathcal{M}_{V,CL}$ model allowed for both H_2O condensation and a partially cloudy atmosphere. We first validated these three models in test retrievals on a simulated 1D low-noise Earth spectrum ($R = 100$, $S/N = 20$). Thereafter, we ran retrievals on LIFE mock observations ($R = 50, 100$; $S/N = 10, 20$) of empirical disk-integrated MIR thermal emission spectra of Earth representative of different views and seasons. The performance of the three models was benchmarked against ground truth averages from remote sensing data.

Independent of the assumed forward model, our retrieval results highlight the unique strength of considering an exoplanet’s MIR thermal emission. Earth-like H_2O , CO_2 , and O_3 concentrations are easily constrained to within ± 1.0 dex, and CH_4 is reliably detected at $R = 100$. Further, we significantly constrain the atmospheric P – T structure (± 0.5 dex for pressures, ± 20 K for temperatures) and the planet radius ($\pm 0.1 R_\oplus$). Yet, our results also demonstrate that simplifying assumptions made by retrieval forward models can bias the characterization. For the $\mathcal{M}_{C,CF}$ model, pressures are underestimated by ~ 0.5 dex, and the abundances of CO_2 , O_3 , and CH_4 overestimated by ≥ 0.6 dex. Also, the obtained R_{pl} estimates are consistently $\geq 0.05 R_\oplus$ too low. This translates to biased equilibrium temperature (T_{eq}) and Bond albedo (A_B) estimates ($T_{eq} \geq 5$ K too high; $A_B \geq 0.05$ too low). With the $\mathcal{M}_{V,CF}$ forward model, these offsets can already be reduced significantly for most parameters. The $\mathcal{M}_{V,CL}$ model yields bias-free estimates for the shape of the P – T structure, R_{pl} , the trace-gas abundances, T_{eq} , and A_B . For the surface pressure P_0 and temperature T_0 , the $\mathcal{M}_{V,CF}$ and $\mathcal{M}_{V,CL}$ retrievals yield lower limits. For both models, the high-pressure atmosphere layers are opaque to MIR radiation due to their high H_2O abundance. Consequentially, these layers do not contribute to the MIR thermal emission spectrum and thus P_0 and T_0 are not constrainable. These results demonstrate that physically motivated forward models can facilitate the accurate interpretation of spectra.

In addition, our work has important implications for the LIFE technical requirements. Konrad et al. (2022) derived preliminary minimal wavelength coverage, R , and S/N re-

quirements by running a grid of retrievals on simulated Earth spectra assuming constant abundance profiles and a cloud-free atmosphere. The authors derived lower requirement limits of $4 - 18.5 \mu m$, $R = 50$, and $S/N = 10$ by requiring a detection of the potential biosignature CH_4 . Yet, our results on empirical Earth spectra suggest, that a bias-free CH_4 detection is not possible for Earth with the current baseline R and S/N requirements. Instead, we find that at $S/N = 10$ a minimal R of 100 is required to ensure a confident and bias-free CH_4 detection. With a proper treatment of the H_2O profile and clouds, an $R = 100$ MIR LIFE observation would allow us to correctly identify an exo-Earth as habitable and quantify the abundance of the biosignature gas CH_4 . Further, our findings suggest that flux measurements above $15.4 \mu m$ and between $4.6 - 6.2 \mu m$ are not essential for an accurate characterization of an exo-Earth with LIFE. However, this must be confirmed for non Earth-like HZ terrestrial exoplanets.

First detailed spectral measurements with the JWST have set us off on a journey to characterize and understand the conditions on terrestrial exoplanets. These efforts will intensify with future generations of optimized space missions like LIFE capable of acquiring detailed spectral measurements of nearby temperate terrestrial exoplanets. Inverse modeling approaches such as atmospheric retrievals will be used to analyze these data. Yet, as we demonstrate, simplifying assumptions in retrievals can lead to a biased interpretation. Studies that extend beyond the Earth scenario are essential to build a profound understanding of how different model assumptions may impact the interpretation of observed exoplanet spectra. These efforts are indispensable steps forward in our pursuit of understanding the habitability of distant worlds and are crucial to identifying signs of life outside the Solar System.

This work has been carried out within the framework of the National Centre of Competence in Research PlanetS supported by the Swiss National Science Foundation under grant 51NF40_205606. S.P.Q. acknowledges the financial support of the SNSF. B.S.K. acknowledges the support of an ETH Zurich Doc.Mobility Fellowship. E.A.’s research was supported by an appointment to the NASA Postdoctoral Program at the NASA Goddard Space Research, administered by Oak Ridge Associated Universities under contract with NASA.

REFERENCES

- AIRS Project. 2020, Aqua/AIRS L3 Monthly Standard Physical Retrieval (AIRS-only) 1 degree x 1 degree V7.0, NASA Goddard Earth Sciences Data and Information Services Center, doi: [10.5067/UBENJB9D3T2H](https://doi.org/10.5067/UBENJB9D3T2H)
- Alei, E., Konrad, B. S., Mollière, P., et al. 2022a, in Society of Photo-Optical Instrumentation Engineers (SPIE) Conference Series, Vol. 12180, Space Telescopes and Instrumentation 2022: Optical, Infrared, and Millimeter Wave, ed. L. E. Coyle, S. Matsuura, & M. D. Perrin, 121803L, doi: [10.1117/12.2631692](https://doi.org/10.1117/12.2631692)

- Alei, E., Konrad, B. S., Angerhausen, D., et al. 2022b, *A&A*, 665, A106, doi: [10.1051/0004-6361/202243760](https://doi.org/10.1051/0004-6361/202243760)
- Alei, E., Quanz, S. P., Konrad, B. S., et al. 2024, arXiv e-prints, arXiv:2406.13037, doi: [10.48550/arXiv.2406.13037](https://doi.org/10.48550/arXiv.2406.13037)
- Angerhausen, D., Ottiger, M., Dannert, F., et al. 2023, *Astrobiology*, 23, 183, doi: [10.1089/ast.2022.0010](https://doi.org/10.1089/ast.2022.0010)
- Angerhausen, D., Pidhorodetska, D., Leung, M., et al. 2024, *AJ*, 167, 128, doi: [10.3847/1538-3881/ad1f4b](https://doi.org/10.3847/1538-3881/ad1f4b)
- Anglada-Escudé, G., Amado, P. J., Barnes, J., et al. 2016, *Nature*, 536, 437, doi: [10.1038/nature19106](https://doi.org/10.1038/nature19106)
- Barstow, J. K., Changeat, Q., Garland, R., et al. 2020, *MNRAS*, 493, 4884, doi: [10.1093/mnras/staa548](https://doi.org/10.1093/mnras/staa548)
- Berta-Thompson, Z. K., Irwin, J., Charbonneau, D., et al. 2015, *Nature*, 527, 204, doi: [10.1038/nature15762](https://doi.org/10.1038/nature15762)
- Borucki, W. J., Koch, D., Basri, G., et al. 2010, *Science*, 327, 977, doi: [10.1126/science.1185402](https://doi.org/10.1126/science.1185402)
- Bowens, R., Meyer, M. R., Delacroix, C., et al. 2021, *A&A*, 653, A8, doi: [10.1051/0004-6361/202141109](https://doi.org/10.1051/0004-6361/202141109)
- Bryson, S., Kunitomo, M., Kopparapu, R. K., et al. 2021, *AJ*, 161, 36, doi: [10.3847/1538-3881/abc418](https://doi.org/10.3847/1538-3881/abc418)
- Buchner, J., Georgakakis, A., Nandra, K., et al. 2014, *A&A*, 564, A125, doi: [10.1051/0004-6361/201322971](https://doi.org/10.1051/0004-6361/201322971)
- Carrión-González, Ó., Kammerer, J., Angerhausen, D., et al. 2023, *A&A*, 678, A96, doi: [10.1051/0004-6361/202347027](https://doi.org/10.1051/0004-6361/202347027)
- Catling, D. C., Krissansen-Totton, J., Kiang, N. Y., et al. 2018, *Astrobiology*, 18, 709, doi: [10.1089/ast.2017.1737](https://doi.org/10.1089/ast.2017.1737)
- Chahine, M. T., PAGANO, T. S., AUMANN, H. H., et al. 2006, *Bulletin of the American Meteorological Society*, 87, 911, doi: [10.1175/BAMS-87-7-911](https://doi.org/10.1175/BAMS-87-7-911)
- Chapman, S. 1932, *Quarterly Journal of the Royal Meteorological Society*, 58, 11, doi: [10.1002/qj.49705824304](https://doi.org/10.1002/qj.49705824304)
- Chen, J., & Kipping, D. 2016, *ApJ*, 834, 17, doi: [10.3847/1538-4357/834/1/17](https://doi.org/10.3847/1538-4357/834/1/17)
- Dannert, F. A., Ottiger, M., Quanz, S. P., et al. 2022, *A&A*, 664, A22, doi: [10.1051/0004-6361/202141958](https://doi.org/10.1051/0004-6361/202141958)
- Des Marais, D. J., Harwit, M. O., Jucks, K. W., et al. 2002, *Astrobiology*, 2, 153, doi: [10.1089/15311070260192246](https://doi.org/10.1089/15311070260192246)
- Dressing, C. D., & Charbonneau, D. 2015, *ApJ*, 807, 45, doi: [10.1088/0004-637X/807/1/45](https://doi.org/10.1088/0004-637X/807/1/45)
- Ertel, S., Defrère, D., Hinz, P., et al. 2020, *AJ*, 159, 177, doi: [10.3847/1538-3881/ab7817](https://doi.org/10.3847/1538-3881/ab7817)
- Feroz, F., Hobson, M. P., & Bridges, M. 2009, *MNRAS*, 398, 1601–1614, doi: [10.1111/j.1365-2966.2009.14548.x](https://doi.org/10.1111/j.1365-2966.2009.14548.x)
- Foreman-Mackey, D., Hogg, D. W., & Morton, T. D. 2014, *ApJ*, 795, 64, doi: [10.1088/0004-637X/795/1/64](https://doi.org/10.1088/0004-637X/795/1/64)
- Frank, F., Jöckel, P., Gromov, S., & Dameris, M. 2018, *Atmospheric Chemistry & Physics*, 18, 9955, doi: [10.5194/acp-18-9955-2018](https://doi.org/10.5194/acp-18-9955-2018)
- Gaudi, B. S., Seager, S., Mennesson, B., et al. 2020, *The Habitable Exoplanet Observatory (HabEx) Mission Concept Study Final Report*, arXiv e-print. <https://arxiv.org/abs/2001.06683>
- Gebhard, T. D., Angerhausen, D., Konrad, B. S., et al. 2023, arXiv e-prints, arXiv:2309.03075, doi: [10.48550/arXiv.2309.03075](https://doi.org/10.48550/arXiv.2309.03075)
- Genthon, C., Piard, L., Vignon, E., et al. 2017, *Atmospheric Chemistry & Physics*, 17, 691, doi: [10.5194/acp-17-691-2017](https://doi.org/10.5194/acp-17-691-2017)
- Gillon, M., Triaud, A. H. M. J., Demory, B.-O., et al. 2017, *Nature*, 542, doi: [10.1038/nature21360](https://doi.org/10.1038/nature21360)
- Goff, J. A. 1957, in the semi-annual meeting of the American Society of Heating and Ventilating Engineers, *Transactions of the American Society of Heating and Ventilating Engineers*, 347 – 354
- Goff, J. A., & Gratch, S. 1946, in the 52nd annual meeting of the American Society of Heating and Ventilating Engineers, *Transactions of the American Society of Heating and Ventilating Engineers*, 95 – 122
- Gordon, I. E., Rothman, L. S., Hargreaves, R. J., et al. 2022, *JQSRT*, 277, 107949, doi: [10.1016/j.jqsrt.2021.107949](https://doi.org/10.1016/j.jqsrt.2021.107949)
- Greene, T. P., Bell, T. J., Ducrot, E., et al. 2023, *Nature*, 618, 39, doi: [10.1038/s41586-023-05951-7](https://doi.org/10.1038/s41586-023-05951-7)
- Hansen, J. T., Ireland, M. J., Laugier, R., & LIFE Collaboration. 2023, *A&A*, 670, A57, doi: [10.1051/0004-6361/202243863](https://doi.org/10.1051/0004-6361/202243863)
- Hansen, J. T., Ireland, M. J., & LIFE Collaboration. 2022, *A&A*, 664, A52, doi: [10.1051/0004-6361/202243107](https://doi.org/10.1051/0004-6361/202243107)
- Harries, J., Carli, B., Rizzi, R., et al. 2008, *Reviews of Geophysics*, 46, RG4004, doi: [10.1029/2007RG000233](https://doi.org/10.1029/2007RG000233)
- Harvey, A. H., Gallagher, J. S., & Sengers, J. M. H. L. 1998, *Journal of Physical and Chemical Reference Data*, 27, 761, doi: [10.1063/1.556029](https://doi.org/10.1063/1.556029)
- Hays, L. E., New, M. H., & Voytek, M. A. 2017, in *LPI Contributions*, Vol. 1989, *Planetary Science Vision 2050 Workshop*, ed. LPI Editorial Board, 8141
- Hearty, T., Song, I., Kim, S., & Tinetti, G. 2009, *The Astrophysical Journal*, 693, 1763. <http://stacks.iop.org/0004-637X/693/i=2/a=1763>
- Hill, M. L., Bott, K., Dalba, P. A., et al. 2023, *The Astronomical Journal*, 165, 34, doi: [10.3847/1538-3881/aca1c0](https://doi.org/10.3847/1538-3881/aca1c0)
- Ih, J., Kempton, E. M. R., Whittaker, E. A., & Lessard, M. 2023, *ApJL*, 952, L4, doi: [10.3847/2041-8213/ace03b](https://doi.org/10.3847/2041-8213/ace03b)
- Jeffreys, H. 1998, *The Theory of Probability*, *Oxford Classic Texts in the Physical Sciences* (OUP Oxford), 432–441
- Jones, R. L., Pyle, J. A., Harries, J. E., et al. 1986, *Quarterly Journal of the Royal Meteorological Society*, 112, 1127, doi: [10.1002/qj.49711247412](https://doi.org/10.1002/qj.49711247412)
- Kammerer, J., & Quanz, S. P. 2018, *A&A*, 609, A4, doi: [10.1051/0004-6361/201731254](https://doi.org/10.1051/0004-6361/201731254)
- Kammerer, J., Quanz, S. P., Dannert, F., & LIFE Collaboration. 2022, *A&A*, 668, A52, doi: [10.1051/0004-6361/202243846](https://doi.org/10.1051/0004-6361/202243846)

- Karman, T., Gordon, I. E., van der Avoird, A., et al. 2019, *Icarus*, 328, 160, doi: <https://doi.org/10.1016/j.icarus.2019.02.034>
- Kasper, M., Cerpa Urrea, N., Pathak, P., et al. 2021, *The Messenger*, 182, 38, doi: [10.18727/0722-6691/5221](https://doi.org/10.18727/0722-6691/5221)
- Kasting, J. F., Whitmire, D. P., & Reynolds, R. T. 1993, *Icarus*, 101, 108, doi: <https://doi.org/10.1006/icar.1993.1010>
- Kofman, V., & Villanueva, G. L. 2021, *JQSRT*, 270, 107708, doi: [10.1016/j.jqsrt.2021.107708](https://doi.org/10.1016/j.jqsrt.2021.107708)
- Kokhanovsky, A., Vountas, M., & Burrows, J. P. 2011, *Remote Sensing*, 3, 836, doi: [10.3390/rs3050836](https://doi.org/10.3390/rs3050836)
- Koll, D. D. B., Malik, M., Mansfield, M., et al. 2019, *ApJ*, 886, 140, doi: [10.3847/1538-4357/ab4c91](https://doi.org/10.3847/1538-4357/ab4c91)
- Konrad, B. S., Alei, E., Quanz, S. P., et al. 2022, *A&A*, 664, A23, doi: [10.1051/0004-6361/202141964](https://doi.org/10.1051/0004-6361/202141964)
- . 2023, *A&A*, 673, A94, doi: [10.1051/0004-6361/202245655](https://doi.org/10.1051/0004-6361/202245655)
- Kopparapu, R. K., Ramirez, R., Kasting, J. F., et al. 2013, *ApJ*, 765, 131, doi: [10.1088/0004-637X/765/2/131](https://doi.org/10.1088/0004-637X/765/2/131)
- Kozakis, T., Mendonça, J. M., & Buchhave, L. A. 2022, *A&A*, 665, A156, doi: [10.1051/0004-6361/202244164](https://doi.org/10.1051/0004-6361/202244164)
- Krissansen-Totton, J., Garland, R., Irwin, P., & Catling, D. C. 2018, *AJ*, 156, 114, doi: [10.3847/1538-3881/aad564](https://doi.org/10.3847/1538-3881/aad564)
- Lim, O., Benneke, B., Doyon, R., et al. 2023, *ApJL*, 955, L22, doi: [10.3847/2041-8213/acf7c4](https://doi.org/10.3847/2041-8213/acf7c4)
- Lincowski, A. P., Meadows, V. S., Zieba, S., et al. 2023, *ApJL*, 955, L7, doi: [10.3847/2041-8213/acee02](https://doi.org/10.3847/2041-8213/acee02)
- Line, M. R., Wolf, A. S., Zhang, X., et al. 2013, *ApJ*, 775, 137, doi: [10.1088/0004-637X/775/2/137](https://doi.org/10.1088/0004-637X/775/2/137)
- Lustig-Yaeger, J., Meadows, V. S., Crisp, D., Line, M. R., & Robinson, T. D. 2023a, arXiv e-prints, arXiv:2308.14804, doi: [10.48550/arXiv.2308.14804](https://doi.org/10.48550/arXiv.2308.14804)
- Lustig-Yaeger, J., Fu, G., May, E. M., et al. 2023b, *Nature Astronomy*, doi: [10.1038/s41550-023-02064-z](https://doi.org/10.1038/s41550-023-02064-z)
- Madhusudhan, N., Sarkar, S., Constantinou, S., et al. 2023, *ApJL*, 956, L13, doi: [10.3847/2041-8213/acf577](https://doi.org/10.3847/2041-8213/acf577)
- Matsuo, T., Dannert, F., Laugier, R., et al. 2023, *A&A*, 678, A97, doi: [10.1051/0004-6361/202345927](https://doi.org/10.1051/0004-6361/202345927)
- Mettler, J.-N., Konrad, B. S., Quanz, S. P., & Helled, R. 2024, *ApJ*, 963, 24, doi: [10.3847/1538-4357/ad198b](https://doi.org/10.3847/1538-4357/ad198b)
- Mettler, J.-N., Quanz, S. P., & Helled, R. 2020, *The Astrophysical Journal*, 160, 246, doi: [10.3847/1538-3881/abc15](https://doi.org/10.3847/1538-3881/abc15)
- Mettler, J.-N., Quanz, S. P., Helled, R., Olson, S. L., & Schwieterman, E. W. 2023, *ApJ*, 946, 82, doi: [10.3847/1538-4357/acbe3c](https://doi.org/10.3847/1538-4357/acbe3c)
- Misra, A., Meadows, V., Claire, M., & Crisp, D. 2014, *Astrobiology*, 14, 67, doi: [10.1089/ast.2013.0990](https://doi.org/10.1089/ast.2013.0990)
- Mollière, P., Wardenier, J. P., van Boekel, R., et al. 2019, *A&A*, 627, A67, doi: [10.1051/0004-6361/201935470](https://doi.org/10.1051/0004-6361/201935470)
- Mollière, P., Stolker, T., Lacour, S., et al. 2020, *A&A*, 640, A131, doi: [10.1051/0004-6361/202038325](https://doi.org/10.1051/0004-6361/202038325)
- Morley, C. V., Kreidberg, L., Rustamkulov, Z., Robinson, T., & Fortney, J. J. 2017, *ApJ*, 850, 121, doi: [10.3847/1538-4357/aa927b](https://doi.org/10.3847/1538-4357/aa927b)
- NASA/GSFC/GMAO Carbon Group. 2021, OCO-2 GEOS Level 3 monthly, 0.5x0.625 assimilated CO2 V10r (OCO2_GEOS.L3CO2.MONTH) at GES DISC, NASA Goddard Earth Sciences Data and Information Services Center
- National Academies of Sciences, Engineering, and Medicine. 2021, *Pathways to Discovery in Astronomy and Astrophysics for the 2020s* (Washington, DC: The National Academies Press), doi: [10.17226/26141](https://doi.org/10.17226/26141)
- Petigura, E. A., Howard, A. W., & Marcy, G. W. 2013, *Proceedings of the National Academy of Science*, 110, 19273, doi: [10.1073/pnas.1319909110](https://doi.org/10.1073/pnas.1319909110)
- Petty, G. W. 2006, *A First Course in Atmospheric Radiation*, 2nd Edition (Madison WI: Sundog Publishing)
- Quanz, S. P., Crossfield, I., Meyer, M. R., Schmalzl, E., & Held, J. 2015, *International Journal of Astrobiology*, 14, 279, doi: [10.1017/S1473550414000135](https://doi.org/10.1017/S1473550414000135)
- Quanz, S. P., Absil, O., Angerhausen, D., et al. 2021, *Experimental Astronomy*, doi: [10.1007/s10686-021-09791-z](https://doi.org/10.1007/s10686-021-09791-z)
- Quanz, S. P., Ottiger, M., Fontanet, E., et al. 2022, *A&A*, 664, A21, doi: [10.1051/0004-6361/202140366](https://doi.org/10.1051/0004-6361/202140366)
- Ribas, I., Bolmont, E., Selsis, F., et al. 2016, *A&A*, 596, A111, doi: [10.1051/0004-6361/201629576](https://doi.org/10.1051/0004-6361/201629576)
- Ricker, G. R., Winn, J. N., Vanderspek, R., et al. 2015, *Journal of Astronomical Telescopes, Instruments, and Systems*, 1, 014003, doi: [10.1117/1.JATIS.1.1.014003](https://doi.org/10.1117/1.JATIS.1.1.014003)
- Robinson, T., & Salvador, A. 2023, *The Planetary Science Journal*, 4, 10, doi: [10.3847/PSJ/acac9a](https://doi.org/10.3847/PSJ/acac9a)
- Rowland, M. J., Morley, C. V., & Line, M. R. 2023, *ApJ*, 947, 6, doi: [10.3847/1538-4357/acbb07](https://doi.org/10.3847/1538-4357/acbb07)
- Rugheimer, S., & Kaltenecker, L. 2018, *The Astrophysical Journal*, 854, 19, doi: [10.3847/1538-4357/aaa47a](https://doi.org/10.3847/1538-4357/aaa47a)
- Schwieterman, E. W., Robinson, T. D., Meadows, V. S., Misra, A., & Domagal-Goldman, S. 2015, *ApJ*, 810, 57, doi: [10.1088/0004-637X/810/1/57](https://doi.org/10.1088/0004-637X/810/1/57)
- Schwieterman, E. W., Kiang, N. Y., Parenteau, M. N., et al. 2018, *Astrobiology*, 18, 663–708, doi: [10.1089/ast.2017.1729](https://doi.org/10.1089/ast.2017.1729)
- Skilling, J. 2006, *Bayesian Anal.*, 1, 833, doi: [10.1214/06-BA127](https://doi.org/10.1214/06-BA127)
- Sneep, M., & Ubachs, W. 2005, *JQSRT*, 92, 293, doi: [10.1016/j.jqsrt.2004.07.025](https://doi.org/10.1016/j.jqsrt.2004.07.025)
- Spichtinger, P., Gierens, K., & Read, W. 2003, *Quarterly Journal of the Royal Meteorological Society*, 129, 3391, doi: [10.1256/qj.02.141](https://doi.org/10.1256/qj.02.141)
- Thalman, R., Zarzana, K. J., Tolbert, M. A., & Volkamer, R. 2014, *JQSRT*, 147, 171, doi: [10.1016/j.jqsrt.2014.05.030](https://doi.org/10.1016/j.jqsrt.2014.05.030)
- . 2017, *JQSRT*, 189, 281, doi: [10.1016/j.jqsrt.2016.12.014](https://doi.org/10.1016/j.jqsrt.2016.12.014)
- The LUVUOIR Team. 2019, arXiv e-prints, arXiv:1912.06219, <https://arxiv.org/abs/1912.06219>

Tinetti, G., Meadows, V. S., Crisp, D., et al. 2006, *Astrobiology*, 6, 34, doi: [10.1089/ast.2006.6.34](https://doi.org/10.1089/ast.2006.6.34)

Vanderspek, R., Huang, C. X., Vanderburg, A., et al. 2019, *ApJL*, 871, L24, doi: [10.3847/2041-8213/aafb7a](https://doi.org/10.3847/2041-8213/aafb7a)

Voyage 2050 Senior Committee. 2021, *Voyage 2050 – Final Recommendations from the Voyage 2050 Senior Committee*. <https://www.cosmos.esa.int/web/voyage-2050>

Wordsworth, R. D., & Pierrehumbert, R. T. 2013, *ApJ*, 778, 154, doi: [10.1088/0004-637X/778/2/154](https://doi.org/10.1088/0004-637X/778/2/154)

Zechmeister, M., Dreizler, S., Ribas, I., et al. 2019, *A&A*, 627, A49, doi: [10.1051/0004-6361/201935460](https://doi.org/10.1051/0004-6361/201935460)

Zieba, S., Kreidberg, L., Ducrot, E., et al. 2023, *Nature*, 620, 746, doi: [10.1038/s41586-023-06232-z](https://doi.org/10.1038/s41586-023-06232-z)

APPENDIX

A. SUPPLEMENTARY DATA FROM THE RETRIEVALS

In Table A1 we list the log-evidences $\ln(\mathcal{Z})$ for all retrievals and the log-Bayes' factors $\log_{10}(K)$ used for model comparison (see Table 1). In Figures A1 and A2, we present the retrieved posteriors for all considered disk-integrated Earth spectra (Figure A1: $S/N = 10$; Figure A2: $S/N = 20$). In Tables A2 to A4, we list all the numeric values corresponding to the posteriors in Figures A1 and A2:

- Table A2 – NP viewing angle posteriors,
- Table A3 – SP viewing angle posteriors,
- Table A4 – EqC viewing angle posteriors.

Table A1. Evidences \mathcal{Z} for all retrieval runs and the resulting Bayes' factors K for model comparison.

Spectrum	R	S/N	Evidence $\ln(\mathcal{Z})$			Bayes' Factor $\log_{10}(K)$		
			$\mathcal{M}_{C,CF}$	$\mathcal{M}_{V,CF}$	$\mathcal{M}_{V,CL}$	$\mathcal{M}_{C,CF}$ vs. $\mathcal{M}_{V,CF}$	$\mathcal{M}_{C,CF}$ vs. $\mathcal{M}_{V,CL}$	$\mathcal{M}_{V,CF}$ vs. $\mathcal{M}_{V,CL}$
Simulated	100	20	$-50.5^{\pm 0.1}$	$-41.9^{\pm 0.1}$	$-40.5^{\pm 0.2}$	$-3.7^{\pm 0.1}$	$-4.3^{\pm 0.1}$	$-0.6^{\pm 0.2}$
NP Jan	50	10	$-25.5^{\pm 0.2}$	$-24.8^{\pm 0.2}$	$-26.1^{\pm 0.2}$	$-0.3^{\pm 0.2}$	$0.3^{\pm 0.2}$	$0.3^{\pm 0.2}$
		20	$-32.4^{\pm 0.2}$	$-31.9^{\pm 0.2}$	$-32.6^{\pm 0.2}$	$-0.2^{\pm 0.2}$	$0.1^{\pm 0.2}$	$0.3^{\pm 0.2}$
	100	10	$-29.4^{\pm 0.2}$	$-29.0^{\pm 0.2}$	$-29.5^{\pm 0.2}$	$-0.2^{\pm 0.2}$	$0.0^{\pm 0.2}$	$0.2^{\pm 0.2}$
		20	$-36.7^{\pm 0.2}$	$-35.7^{\pm 0.2}$	$-35.8^{\pm 0.2}$	$-0.4^{\pm 0.2}$	$-0.5^{\pm 0.2}$	$0.1^{\pm 0.2}$
NP Jul	50	10	$-25.3^{\pm 0.2}$	$-24.4^{\pm 0.2}$	$-25.5^{\pm 0.2}$	$-0.2^{\pm 0.2}$	$-0.1^{\pm 0.2}$	$0.2^{\pm 0.2}$
		20	$-32.7^{\pm 0.2}$	$-32.8^{\pm 0.2}$	$-32.3^{\pm 0.2}$	$0.0^{\pm 0.2}$	$-0.2^{\pm 0.2}$	$-0.2^{\pm 0.2}$
	100	10	$-29.9^{\pm 0.2}$	$-30.7^{\pm 0.2}$	$-29.3^{\pm 0.2}$	$0.3^{\pm 0.2}$	$-0.1^{\pm 0.2}$	$-0.3^{\pm 0.2}$
		20	$-38.4^{\pm 0.2}$	$-38.0^{\pm 0.2}$	$-37.6^{\pm 0.2}$	$-0.2^{\pm 0.2}$	$-0.4^{\pm 0.2}$	$-0.2^{\pm 0.2}$
SP Jan	50	10	$-25.4^{\pm 0.2}$	$-25.8^{\pm 0.2}$	$-25.6^{\pm 0.2}$	$0.2^{\pm 0.2}$	$0.1^{\pm 0.2}$	$-0.1^{\pm 0.2}$
		20	$-32.2^{\pm 0.2}$	$-31.8^{\pm 0.2}$	$-31.8^{\pm 0.2}$	$-0.2^{\pm 0.2}$	$-0.2^{\pm 0.2}$	$-0.0^{\pm 0.2}$
	100	10	$-29.2^{\pm 0.2}$	$-29.1^{\pm 0.2}$	$-29.1^{\pm 0.2}$	$-0.1^{\pm 0.2}$	$-0.1^{\pm 0.2}$	$0.0^{\pm 0.2}$
		20	$-37.1^{\pm 0.2}$	$-36.6^{\pm 0.2}$	$-37.2^{\pm 0.2}$	$-0.2^{\pm 0.2}$	$0.1^{\pm 0.2}$	$0.2^{\pm 0.2}$
SP Jul	50	10	$-25.9^{\pm 0.2}$	$-25.8^{\pm 0.2}$	$-25.9^{\pm 0.2}$	$-0.0^{\pm 0.2}$	$0.0^{\pm 0.2}$	$0.0^{\pm 0.2}$
		20	$-32.5^{\pm 0.2}$	$-31.8^{\pm 0.2}$	$-33.0^{\pm 0.2}$	$-0.3^{\pm 0.2}$	$0.2^{\pm 0.2}$	$0.5^{\pm 0.2}$
	100	10	$-29.6^{\pm 0.2}$	$-29.1^{\pm 0.2}$	$-29.6^{\pm 0.2}$	$-0.2^{\pm 0.2}$	$0.0^{\pm 0.2}$	$0.2^{\pm 0.2}$
		20	$-37.9^{\pm 0.2}$	$-36.8^{\pm 0.2}$	$-37.6^{\pm 0.2}$	$-0.5^{\pm 0.2}$	$-0.1^{\pm 0.2}$	$0.3^{\pm 0.2}$
EqC Jan	50	10	$-25.4^{\pm 0.2}$	$-25.5^{\pm 0.2}$	$-25.6^{\pm 0.2}$	$0.0^{\pm 0.2}$	$0.1^{\pm 0.2}$	$-0.0^{\pm 0.2}$
		20	$-32.7^{\pm 0.2}$	$-32.8^{\pm 0.2}$	$-32.1^{\pm 0.2}$	$0.1^{\pm 0.2}$	$-0.3^{\pm 0.2}$	$-0.3^{\pm 0.2}$
	100	10	$-29.4^{\pm 0.2}$	$-29.4^{\pm 0.2}$	$-29.6^{\pm 0.2}$	$-0.0^{\pm 0.2}$	$0.1^{\pm 0.2}$	$0.1^{\pm 0.2}$
		20	$-38.3^{\pm 0.2}$	$-37.1^{\pm 0.2}$	$-38.0^{\pm 0.2}$	$-0.5^{\pm 0.2}$	$-0.1^{\pm 0.2}$	$0.4^{\pm 0.2}$
EqC Jul	50	10	$-25.4^{\pm 0.2}$	$-26.2^{\pm 0.2}$	$-25.6^{\pm 0.2}$	$0.3^{\pm 0.2}$	$0.1^{\pm 0.2}$	$-0.2^{\pm 0.2}$
		20	$-33.8^{\pm 0.2}$	$-33.9^{\pm 0.2}$	$-32.6^{\pm 0.2}$	$0.0^{\pm 0.2}$	$-0.2^{\pm 0.2}$	$-0.3^{\pm 0.2}$
	100	10	$-29.4^{\pm 0.2}$	$-29.6^{\pm 0.2}$	$-29.9^{\pm 0.2}$	$0.1^{\pm 0.2}$	$0.2^{\pm 0.2}$	$0.1^{\pm 0.2}$
		20	$-38.6^{\pm 0.2}$	$-37.1^{\pm 0.2}$	$-38.4^{\pm 0.2}$	$-0.6^{\pm 0.2}$	$-0.1^{\pm 0.2}$	$0.6^{\pm 0.2}$

NOTE—The $\log_{10}(K)$ values were calculated from $\ln(\mathcal{Z})$ using Equation (1) from Section 2.1.

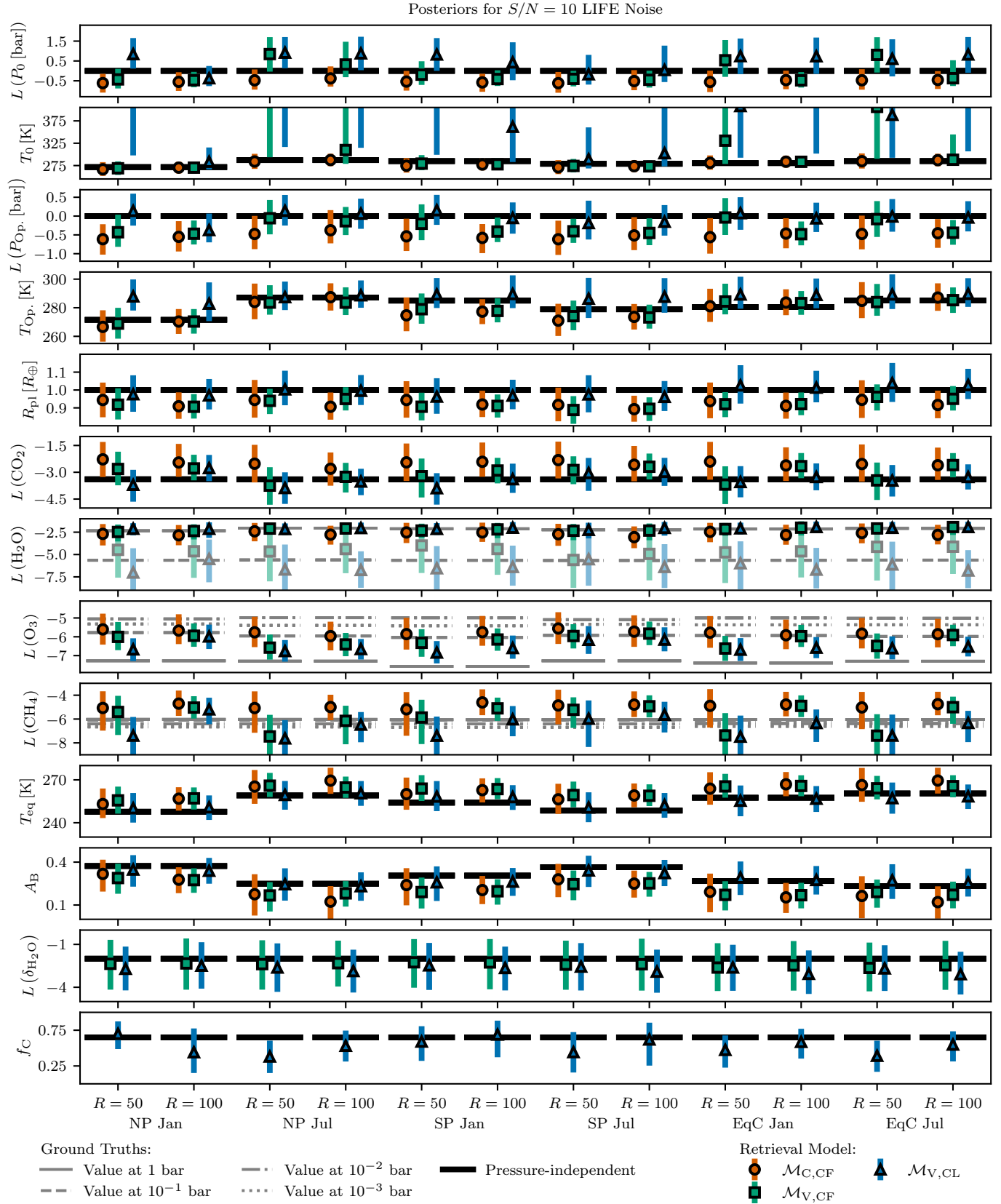


Figure A1. Posteriors from retrievals on the six disk-integrated Earth spectra for the $S/N = 10$ LIFESIM-noise scenarios. Here, $L(\cdot)$ stands for $\log_{10}(\cdot)$. Thick black lines indicate pressure-independent ground truths. Thin gray lines show the ground truth abundances at different atmospheric pressures (solid: 1 bar; dashed: 10^{-1} bar; dashed-dotted: 10^{-2} bar; dotted: 10^{-3} bar). The markers represent the retrieval models: orange circles – $\mathcal{M}_{C,CF}$, green squares – $\mathcal{M}_{V,CF}$, and blue triangles – $\mathcal{M}_{V,CL}$. The colored lines indicate the 16% – 84% posterior percentiles. For the $\mathcal{M}_{V,CF}$ and $\mathcal{M}_{V,CL}$ models, which assume variable H_2O profiles, we provide both the retrieved H_2O abundance at the pressure P_{Op} , where the atmosphere becomes optically thick (dark marker color) and at 1 dex below P_{Op} . (light marker color).

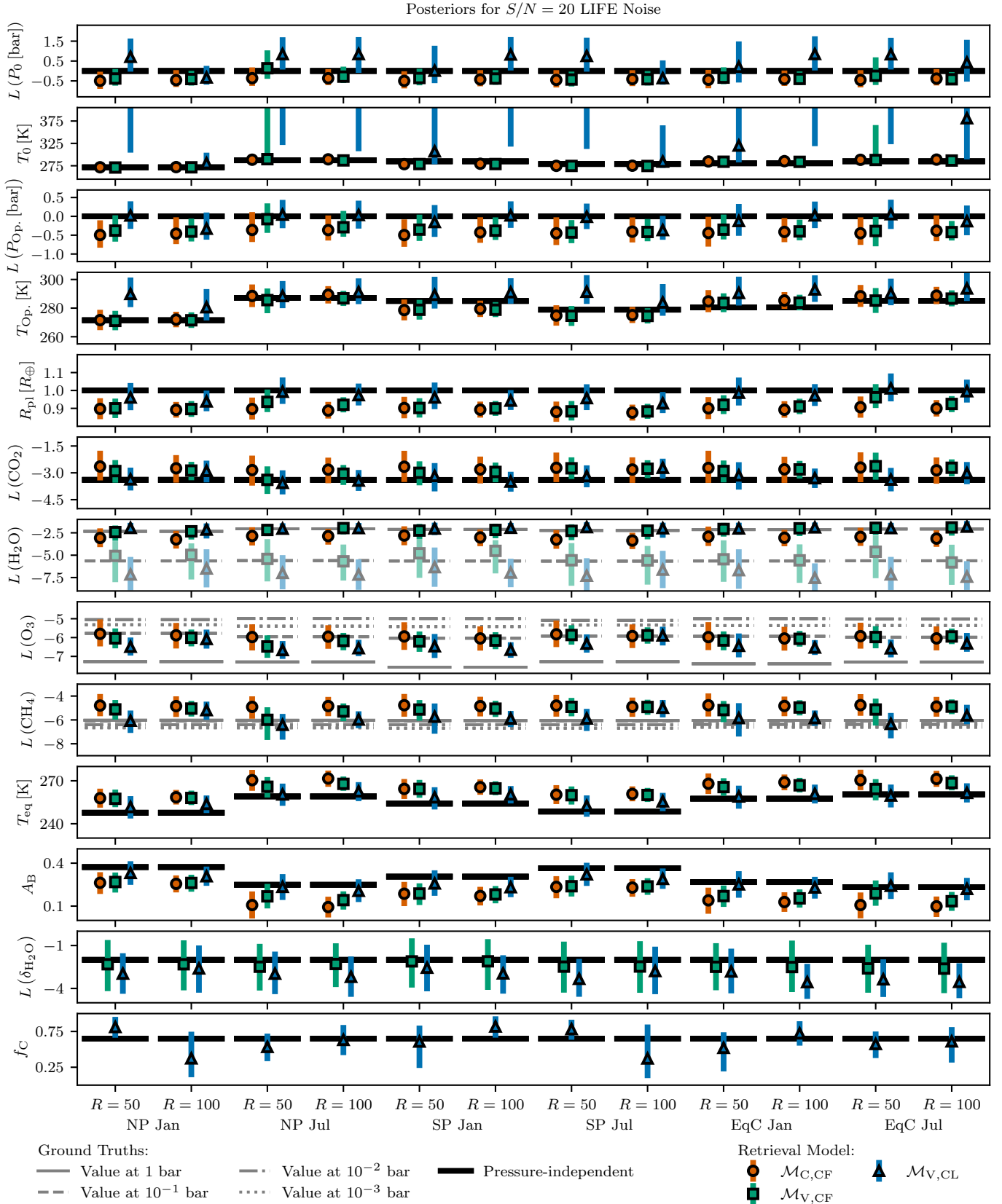


Figure A2. Posteriors from retrievals on the six disk-integrated Earth spectra for the $S/N = 20$ LIFESIM-noise scenarios. Here, $L(\cdot)$ stands for $\log_{10}(\cdot)$. Thick black lines indicate pressure-independent ground truths. Thin gray lines show the ground truth abundances at different atmospheric pressures (solid: 1 bar; dashed: 10^{-1} bar; dashed-dotted: 10^{-2} bar; dotted: 10^{-3} bar). The markers represent the retrieval models: orange circles – $\mathcal{M}_{C,CF}$, green squares – $\mathcal{M}_{V,CF}$, and blue triangles – $\mathcal{M}_{V,CL}$. The colored lines indicate the 16% – 84% posterior percentiles. For the $\mathcal{M}_{V,CF}$ and $\mathcal{M}_{V,CL}$ models, which assume variable H_2O profiles, we provide both the retrieved H_2O abundance at the pressure P_{Op} , where the atmosphere becomes optically thick (dark marker color) and at 1 dex below P_{Op} (light marker color).

Table A2. Numeric values for the NP view posteriors shown in Figures A1 and A2.

Parameter	Ground Truths						Posteriors for $R = 50$ Spectra						Posteriors for $R = 100$ Spectra					
	Pressure Levels [bar]			10^{-3}			LIFEsim $S/N = 10$			LIFEsim $S/N = 20$			LIFEsim $S/N = 10$			LIFEsim $S/N = 20$		
	1	10^{-1}	10^{-2}	$M_{C,CF}$	$M_{V,CF}$	$M_{V,CL}$	$M_{C,CF}$	$M_{V,CF}$	$M_{V,CL}$									
$L(P_0$ [bar])	0.0	0.0	0.0	-0.6 ^{+0.3} _{-0.3}	-0.4 ^{+0.4} _{-0.3}	0.8 ^{+0.7} _{-0.6}	-0.5 ^{+0.3} _{-0.3}	-0.4 ^{+0.3} _{-0.2}	0.7 ^{+0.8} _{-0.6}	-0.6 ^{+0.3} _{-0.3}	-0.5 ^{+0.3} _{-0.3}	-0.4 ^{+0.5} _{-0.3}	-0.5 ^{+0.4} _{-0.2}	-0.4 ^{+0.5} _{-0.3}	-0.5 ^{+0.4} _{-0.2}	-0.4 ^{+0.3} _{-0.2}	-0.3 ^{+0.4} _{-0.2}	
$L(P_{Op}$ [bar])	0.0	0.0	0.0	-0.6 ^{+0.3} _{-0.3}	-0.4 ^{+0.4} _{-0.3}	0.1 ^{+0.4} _{-0.3}	-0.5 ^{+0.3} _{-0.3}	-0.4 ^{+0.3} _{-0.2}	0.0 ^{+0.3} _{-0.3}	-0.6 ^{+0.3} _{-0.3}	-0.6 ^{+0.3} _{-0.3}	-0.4 ^{+0.4} _{-0.3}	-0.5 ^{+0.3} _{-0.2}	-0.4 ^{+0.4} _{-0.3}	-0.5 ^{+0.4} _{-0.2}	-0.4 ^{+0.3} _{-0.2}	-0.3 ^{+0.4} _{-0.2}	
T_0 [K]	272	269 ⁺¹⁰ ₋₈	269 ⁺⁹ ₋₉	267 ⁺¹⁰ ₋₈	269 ⁺⁹ ₋₉	453 ⁺⁴⁰² ₋₁₄₈	272 ⁺⁵ ₋₅	271 ⁺⁵ ₋₅	448 ⁺⁴⁶⁵ ₋₁₃₇	270 ⁺⁷ ₋₇	270 ⁺⁷ ₋₇	283 ⁺²⁶ ₋₁₁	270 ⁺⁷ ₋₆	283 ⁺¹³ ₋₁₀	272 ⁺³ ₋₃	272 ⁺³ ₋₃	281 ⁺⁷ ₋₇	
T_{Op} [K]	272	267 ⁺¹⁰ ₋₈	269 ⁺⁹ ₋₉	267 ⁺¹⁰ ₋₈	269 ⁺⁹ ₋₉	288 ⁺¹⁰ ₋₈	272 ⁺⁵ ₋₅	271 ⁺⁵ ₋₅	290 ⁺¹⁰ ₋₇	270 ⁺⁷ ₋₇	270 ⁺⁷ ₋₇	283 ⁺¹³ ₋₁₀	270 ⁺⁷ ₋₆	283 ⁺¹⁰ ₋₇	272 ⁺³ ₋₃	272 ⁺³ ₋₃	281 ⁺¹¹ ₋₇	
R_{pl} [R_{\oplus}]	1.0	0.9 ^{+0.1} _{-0.1}	0.9 ^{+0.1} _{-0.1}	0.9 ^{+0.1} _{-0.1}	0.9 ^{+0.1} _{-0.1}	1.0 ^{+0.1} _{-0.1}	0.9 ^{+0.0} _{-0.0}	0.9 ^{+0.0} _{-0.0}	1.0 ^{+0.1} _{-0.1}	0.9 ^{+0.1} _{-0.1}	0.9 ^{+0.1} _{-0.1}	1.0 ^{+0.1} _{-0.1}	0.9 ^{+0.1} _{-0.1}	1.0 ^{+0.1} _{-0.1}	0.9 ^{+0.0} _{-0.0}	0.9 ^{+0.0} _{-0.0}	0.9 ^{+0.0} _{-0.0}	
$L(CO_2)$	-3.4	-2.3 ^{+0.8} _{-0.8}	-2.8 ^{+0.8} _{-0.8}	-2.3 ^{+0.8} _{-0.8}	-2.8 ^{+0.8} _{-0.8}	-3.7 ^{+0.7} _{-0.8}	-2.6 ^{+0.7} _{-0.6}	-2.9 ^{+0.5} _{-0.5}	-3.4 ^{+0.5} _{-0.5}	-2.5 ^{+0.9} _{-0.6}	-2.5 ^{+0.9} _{-0.6}	-2.8 ^{+0.6} _{-0.6}	-2.8 ^{+0.6} _{-0.6}	-2.8 ^{+0.6} _{-0.6}	-2.9 ^{+0.3} _{-0.4}	-2.9 ^{+0.3} _{-0.4}	-2.9 ^{+0.4} _{-0.5}	
$L(O_3)$	-7.3	-5.8	-5.0	-5.3	-6.0 ^{+0.7} _{-0.6}	-6.7 ^{+0.4} _{-0.5}	-5.8 ^{+0.6} _{-0.5}	-6.0 ^{+0.4} _{-0.4}	-6.5 ^{+0.3} _{-0.3}	-5.7 ^{+0.7} _{-0.6}	-5.9 ^{+0.5} _{-0.4}	-6.0 ^{+0.5} _{-0.5}	-5.9 ^{+0.5} _{-0.5}	-6.0 ^{+0.5} _{-0.5}	-6.0 ^{+0.3} _{-0.3}	-6.1 ^{+0.3} _{-0.4}	-6.1 ^{+0.3} _{-0.4}	
$L(CH_4)$	-6.0	-6.1	-6.4	-6.7	-5.1 ^{+1.2} _{-1.1}	-5.4 ^{+1.1} _{-1.1}	-4.8 ^{+0.7} _{-0.7}	-5.1 ^{+0.5} _{-0.6}	-6.1 ^{+0.6} _{-0.6}	-4.7 ^{+0.9} _{-0.8}	-5.0 ^{+0.7} _{-0.7}	-5.2 ^{+0.7} _{-1.0}	-4.8 ^{+0.6} _{-0.7}	-5.0 ^{+0.4} _{-0.4}	-5.0 ^{+0.4} _{-0.4}	-5.2 ^{+0.5} _{-0.6}	-5.2 ^{+0.5} _{-0.6}	
$L(H_2O)$	-2.3	-5.6	-2.5 ^{+0.7} _{-0.7}	-2.1 ^{+0.3} _{-0.4}	-3.1 ^{+0.8} _{-0.7}	-2.4 ^{+0.4} _{-0.4}	-2.0 ^{+0.3} _{-0.3}	-2.8 ^{+0.8} _{-0.8}	-2.4 ^{+0.4} _{-0.4}	-2.1 ^{+0.4} _{-0.4}	-2.8 ^{+0.8} _{-0.8}	-2.1 ^{+0.4} _{-0.4}	-2.3 ^{+0.6} _{-0.6}	-2.1 ^{+0.4} _{-0.4}	-2.1 ^{+0.4} _{-0.4}	
$L(\delta_{H_2O})$	-2.0	-2.4 ^{+1.5} _{-1.6}	-2.4 ^{+1.5} _{-1.6}	...	-2.4 ^{+1.5} _{-1.6}	-2.7 ^{+1.4} _{-1.3}	...	-2.3 ^{+1.5} _{-1.7}	-3.0 ^{+1.2} _{-1.2}	...	-2.3 ^{+1.5} _{-1.6}	-2.5 ^{+1.4} _{-1.4}	-2.3 ^{+1.5} _{-1.6}	-2.5 ^{+1.4} _{-1.4}	-2.3 ^{+1.5} _{-1.6}	-2.3 ^{+1.5} _{-1.6}	-2.3 ^{+1.5} _{-1.6}	
f_c	0.7	0.7 ^{+0.1} _{-0.2}	0.8 ^{+0.1} _{-0.1}	0.4 ^{+0.3} _{-0.2}	...	0.4 ^{+0.3} _{-0.2}	...	0.4 ^{+0.3} _{-0.2}	0.4 ^{+0.3} _{-0.2}	
T_{eq} [K]	248	253 ⁺⁹ ₋₈	256 ⁺⁸ ₋₇	253 ⁺⁹ ₋₈	256 ⁺⁸ ₋₇	250 ⁺⁹ ₋₈	258 ⁺⁵ ₋₅	257 ⁺⁴ ₋₄	252 ⁺⁶ ₋₆	257 ⁺⁶ ₋₆	257 ⁺⁶ ₋₆	251 ⁺⁶ ₋₇	257 ⁺⁶ ₋₆	251 ⁺⁶ ₋₇	258 ⁺³ ₋₃	258 ⁺³ ₋₃	254 ⁺⁴ ₋₄	
A_B	0.37	0.32 ^{+0.08} _{-0.10}	0.29 ^{+0.08} _{-0.09}	0.32 ^{+0.08} _{-0.10}	0.29 ^{+0.08} _{-0.09}	0.35 ^{+0.08} _{-0.10}	0.26 ^{+0.05} _{-0.06}	0.27 ^{+0.05} _{-0.06}	0.33 ^{+0.06} _{-0.06}	0.28 ^{+0.07} _{-0.07}	0.27 ^{+0.06} _{-0.07}	0.34 ^{+0.07} _{-0.07}	0.27 ^{+0.06} _{-0.07}	0.34 ^{+0.07} _{-0.07}	0.26 ^{+0.04} _{-0.04}	0.26 ^{+0.04} _{-0.04}	0.31 ^{+0.05} _{-0.05}	
$L(P_0$ [bar])	0.0	-0.5 ^{+0.4} _{-0.3}	0.8 ^{+0.7} _{-0.6}	-0.5 ^{+0.3} _{-0.3}	0.8 ^{+0.7} _{-0.6}	0.9 ^{+0.6} _{-0.6}	-0.4 ^{+0.4} _{-0.2}	0.1 ^{+0.8} _{-0.4}	0.8 ^{+0.7} _{-0.6}	-0.4 ^{+0.5} _{-0.3}	-0.4 ^{+0.5} _{-0.3}	0.9 ^{+0.7} _{-0.7}	-0.4 ^{+0.3} _{-0.2}	0.9 ^{+0.7} _{-0.7}	-0.4 ^{+0.3} _{-0.2}	-0.3 ^{+0.4} _{-0.2}	0.8 ^{+0.7} _{-0.6}	
$L(P_{Op}$ [bar])	0.0	-0.5 ^{+0.4} _{-0.3}	-0.1 ^{+0.4} _{-0.4}	-0.5 ^{+0.3} _{-0.3}	-0.1 ^{+0.4} _{-0.4}	0.1 ^{+0.3} _{-0.3}	-0.4 ^{+0.4} _{-0.2}	-0.1 ^{+0.3} _{-0.3}	0.0 ^{+0.3} _{-0.3}	-0.4 ^{+0.5} _{-0.3}	-0.4 ^{+0.5} _{-0.3}	0.1 ^{+0.3} _{-0.3}	-0.4 ^{+0.3} _{-0.2}	0.1 ^{+0.3} _{-0.3}	-0.4 ^{+0.3} _{-0.2}	-0.3 ^{+0.4} _{-0.2}	0.0 ^{+0.3} _{-0.3}	
T_0 [K]	287	284 ⁺¹¹ ₋₁₀	440 ⁺⁰⁶ ₋₁₄₀	284 ⁺¹¹ ₋₁₀	440 ⁺⁰⁶ ₋₁₄₀	477 ⁺⁰³ ₋₁₅₄	289 ⁺⁶ ₋₆	290 ⁺¹⁵⁴ ₋₆	484 ⁺⁰⁵ ₋₁₅₆	287 ⁺⁸ ₋₇	287 ⁺⁸ ₋₇	482 ⁺⁴³³ ₋₁₆₁	310 ⁺²⁸¹ ₋₂₅	482 ⁺⁴³³ ₋₁₆₁	289 ⁺⁴ ₋₄	287 ⁺³ ₋₃	487 ⁺⁴⁵⁶ ₋₁₇₄	
T_{Op} [K]	287	284 ⁺¹⁰ ₋₁₀	284 ⁺¹⁰ ₋₆	284 ⁺¹⁰ ₋₆	284 ⁺¹⁰ ₋₆	287 ⁺⁹ ₋₇	289 ⁺⁶ ₋₆	286 ⁺⁶ ₋₆	288 ⁺⁸ ₋₆	287 ⁺⁸ ₋₇	284 ⁺⁹ ₋₇	289 ⁺⁸ ₋₇	284 ⁺⁹ ₋₇	289 ⁺⁸ ₋₇	289 ⁺⁴ ₋₄	287 ⁺³ ₋₃	291 ⁺⁸ ₋₆	
R_{pl} [R_{\oplus}]	1.0	0.9 ^{+0.1} _{-0.1}	0.9 ^{+0.1} _{-0.1}	0.9 ^{+0.1} _{-0.1}	0.9 ^{+0.1} _{-0.1}	1.0 ^{+0.1} _{-0.1}	0.9 ^{+0.0} _{-0.0}	0.9 ^{+0.1} _{-0.0}	1.0 ^{+0.1} _{-0.1}	0.9 ^{+0.1} _{-0.1}	0.9 ^{+0.1} _{-0.1}	1.0 ^{+0.1} _{-0.1}	0.9 ^{+0.1} _{-0.0}	1.0 ^{+0.1} _{-0.1}	0.9 ^{+0.0} _{-0.0}	0.9 ^{+0.0} _{-0.0}	1.0 ^{+0.0} _{-0.0}	
$L(CO_2)$	-3.4	-2.5 ^{+0.9} _{-0.9}	-3.7 ^{+0.9} _{-0.9}	-2.5 ^{+0.9} _{-0.9}	-3.7 ^{+0.9} _{-0.9}	-3.9 ^{+0.7} _{-0.7}	-2.8 ^{+0.6} _{-0.6}	-3.4 ^{+0.6} _{-0.6}	-3.6 ^{+0.5} _{-0.5}	-2.8 ^{+0.8} _{-0.8}	-2.8 ^{+0.8} _{-0.8}	-3.5 ^{+0.6} _{-0.6}	-3.3 ^{+0.7} _{-0.7}	-3.5 ^{+0.6} _{-0.6}	-2.8 ^{+0.5} _{-0.6}	-3.0 ^{+0.3} _{-0.4}	-3.4 ^{+0.4} _{-0.4}	
$L(O_3)$	-7.3	-6.0	-5.0	-5.4	-6.6 ^{+0.5} _{-0.5}	-6.8 ^{+0.4} _{-0.4}	-6.0 ^{+0.5} _{-0.6}	-6.5 ^{+0.4} _{-0.5}	-6.7 ^{+0.3} _{-0.3}	-6.0 ^{+0.6} _{-0.6}	-6.0 ^{+0.6} _{-0.6}	-6.4 ^{+0.5} _{-0.5}	-6.4 ^{+0.5} _{-0.5}	-6.7 ^{+0.4} _{-0.4}	-6.0 ^{+0.5} _{-0.5}	-6.2 ^{+0.3} _{-0.3}	-6.6 ^{+0.3} _{-0.3}	
$L(CH_4)$	-6.0	-6.1	-6.4	-6.7	-5.1 ^{+1.2} _{-1.1}	-7.6 ^{+1.3} _{-1.4}	-4.9 ^{+0.6} _{-0.6}	-6.0 ^{+0.8} _{-0.8}	-6.4 ^{+0.7} _{-1.0}	-5.0 ^{+0.8} _{-0.9}	-5.0 ^{+0.8} _{-0.9}	-6.2 ^{+1.0} _{-1.2}	-6.2 ^{+1.0} _{-1.2}	-6.5 ^{+0.8} _{-1.0}	-4.8 ^{+0.5} _{-0.6}	-5.3 ^{+0.4} _{-0.6}	-6.0 ^{+0.5} _{-0.5}	
$L(H_2O)$	-2.1	-5.6	-2.1 ^{+0.4} _{-0.4}	-2.2 ^{+0.3} _{-0.3}	-2.9 ^{+0.7} _{-0.7}	-2.2 ^{+0.4} _{-0.4}	-2.0 ^{+0.3} _{-0.3}	-2.8 ^{+0.8} _{-0.8}	-2.8 ^{+0.8} _{-0.8}	-2.0 ^{+0.3} _{-0.3}	-2.1 ^{+0.3} _{-0.4}	-2.0 ^{+0.3} _{-0.3}	-2.9 ^{+0.5} _{-0.6}	-2.0 ^{+0.3} _{-0.4}	-2.0 ^{+0.3} _{-0.2}	
$L(\delta_{H_2O})$	-2.0	-2.4 ^{+1.5} _{-1.6}	-2.4 ^{+1.5} _{-1.6}	...	-2.4 ^{+1.5} _{-1.6}	-2.6 ^{+1.5} _{-1.5}	...	-2.5 ^{+1.4} _{-1.5}	-3.0 ^{+1.3} _{-1.2}	...	-2.3 ^{+1.4} _{-1.4}	-2.9 ^{+1.3} _{-1.3}	-2.3 ^{+1.4} _{-1.4}	-2.9 ^{+1.3} _{-1.3}	-2.3 ^{+1.4} _{-1.4}	-2.3 ^{+1.4} _{-1.4}	-3.2 ^{+1.2} _{-1.2}	
f_c	0.7	0.4 ^{+0.2} _{-0.2}	0.5 ^{+0.1} _{-0.2}	0.5 ^{+0.2} _{-0.2}	...	0.5 ^{+0.2} _{-0.2}	0.6 ^{+0.2} _{-0.2}	
T_{eq} [K]	259	265 ⁺¹⁰ ₋₁₀	266 ⁺⁷ ₋₆	265 ⁺¹⁰ ₋₁₀	266 ⁺⁷ ₋₆	259 ⁺⁸ ₋₈	270 ⁺⁵ ₋₅	266 ⁺⁵ ₋₆	260 ⁺⁶ ₋₆	269 ⁺⁷ ₋₇	265 ⁺⁶ ₋₅	261 ⁺⁷ ₋₇	265 ⁺⁶ ₋₅	261 ⁺⁷ ₋₇	272 ⁺⁴ ₋₄	268 ⁺³ ₋₃	263 ⁺⁴ ₋₅	
A_B	0.25	0.18 ^{+0.12} _{-0.13}	0.17 ^{+0.07} _{-0.09}	0.18 ^{+0.12} _{-0.13}	0.17 ^{+0.07} _{-0.09}	0.25 ^{+0.09} _{-0.09}	0.11 ^{+0.08} _{-0.07}	0.17 ^{+0.08} _{-0.06}	0.23 ^{+0.07} _{-0.07}	0.12 ^{+0.09} _{-0.10}	0.18 ^{+0.09} _{-0.07}	0.23 ^{+0.08} _{-0.08}	0.18 ^{+0.09} _{-0.10}	0.23 ^{+0.08} _{-0.08}	0.09 ^{+0.05} _{-0.05}	0.14 ^{+0.04} _{-0.05}	0.21 ^{+0.06} _{-0.06}	

NOTE—Here, $L(\cdot)$ stands for $\log_{10}(\cdot)$. In columns two to five, we list the ground truth values for the view. If independent of the atmospheric pressure, we provide a single value. Otherwise, we provide ground truth values at 1 bar, 10^{-1} bar, 10^{-2} bar, and 10^{-3} bar where available. In the last twelve columns, we list the median and the 16% – 84% range (via +/– indices) of the parameter posteriors for all combinations of R (50, 100), S/N (10, 20), and retrieval model ($M_{C,CF}$, $M_{V,CF}$, $M_{V,CL}$). For H_2O , all listed posterior values correspond to the abundances at the pressure P_{Op} , where the atmosphere becomes optically thick.

Table A3. Numeric values for the SP view posteriors shown in Figures A1 and A2.

Parameter	Ground Truths				Posteriors for $R = 50$ Spectra						Posteriors for $R = 100$ Spectra					
	Pressure Levels [bar]				LIFEsim $S/N = 10$			LIFEsim $S/N = 20$			LIFEsim $S/N = 10$			LIFEsim $S/N = 20$		
	1	10^{-1}	10^{-2}	10^{-3}	$M_{C,CF}$	$M_{V,CF}$	$M_{V,CL}$	$M_{C,CF}$	$M_{V,CF}$	$M_{V,CL}$	$M_{C,CF}$	$M_{V,CF}$	$M_{V,CL}$	$M_{C,CF}$	$M_{V,CF}$	$M_{V,CL}$
$L(P_0)$ [bar]	0.0				$-0.5^{+0.4}_{-0.3}$	$-0.2^{+0.5}_{-0.4}$	$0.8^{+0.7}_{-0.7}$	$-0.5^{+0.3}_{-0.2}$	$-0.4^{+0.3}_{-0.2}$	$0.0^{+1.1}_{-0.5}$	$-0.6^{+0.3}_{-0.3}$	$-0.4^{+0.3}_{-0.2}$	$0.4^{+0.9}_{-0.8}$	$-0.4^{+0.3}_{-0.2}$	$-0.4^{+0.3}_{-0.2}$	$0.8^{+0.7}_{-0.7}$
$L(P_{Op})$ [bar]	0.0				$-0.5^{+0.4}_{-0.3}$	$-0.2^{+0.4}_{-0.4}$	$0.2^{+0.3}_{-0.3}$	$-0.5^{+0.3}_{-0.2}$	$-0.4^{+0.3}_{-0.2}$	$-0.2^{+0.4}_{-0.3}$	$-0.6^{+0.3}_{-0.3}$	$-0.4^{+0.3}_{-0.2}$	$-0.1^{+0.3}_{-0.3}$	$-0.4^{+0.3}_{-0.2}$	$-0.4^{+0.3}_{-0.2}$	$0.0^{+0.3}_{-0.3}$
T_0 [K]	285				275^{+10}_{-9}	279^{+13}_{-8}	439^{+369}_{-133}	279^{+5}_{-5}	279^{+5}_{-5}	307^{+297}_{-23}	277^{+7}_{-7}	278^{+7}_{-6}	362^{+407}_{-4}	279^{+4}_{-3}	279^{+3}_{-3}	504^{+513}_{-179}
T_{Op} [K]	285				275^{+11}_{-9}	279^{+9}_{-8}	289^{+10}_{-7}	279^{+5}_{-5}	279^{+5}_{-5}	289^{+11}_{-8}	277^{+7}_{-7}	278^{+7}_{-6}	290^{+11}_{-8}	279^{+4}_{-3}	279^{+3}_{-3}	291^{+8}_{-6}
R_{pl} [R_{\oplus}]	1.0				$0.9^{+0.1}_{-0.1}$	$0.9^{+0.1}_{-0.1}$	$1.0^{+0.1}_{-0.1}$	$0.9^{+0.0}_{-0.0}$	$0.9^{+0.0}_{-0.0}$	$1.0^{+0.1}_{-0.0}$	$0.9^{+0.1}_{-0.1}$	$0.9^{+0.0}_{-0.0}$	$1.0^{+0.1}_{-0.0}$	$0.9^{+0.0}_{-0.0}$	$0.9^{+0.0}_{-0.0}$	$0.9^{+0.0}_{-0.0}$
$L(CO_2)$	-3.4				$-2.4^{+0.9}_{-0.9}$	$-3.2^{+0.8}_{-1.0}$	$-3.9^{+0.7}_{-0.8}$	$-2.7^{+0.7}_{-0.7}$	$-3.0^{+0.5}_{-0.5}$	$-3.2^{+0.6}_{-0.7}$	$-2.4^{+0.9}_{-0.7}$	$-2.9^{+0.5}_{-0.6}$	$-3.4^{+0.7}_{-0.6}$	$-2.8^{+0.6}_{-0.6}$	$-2.9^{+0.4}_{-0.4}$	$-3.5^{+0.4}_{-0.4}$
$L(O_3)$	-7.6	-6.0	-5.0	-5.4	$-5.9^{+0.7}_{-0.7}$	$-6.3^{+0.6}_{-0.6}$	$-6.8^{+0.5}_{-0.4}$	$-5.9^{+0.6}_{-0.6}$	$-6.2^{+0.4}_{-0.4}$	$-6.5^{+0.5}_{-0.5}$	$-5.8^{+0.7}_{-0.6}$	$-6.1^{+0.4}_{-0.4}$	$-6.6^{+0.5}_{-0.4}$	$-6.0^{+0.5}_{-0.5}$	$-6.2^{+0.3}_{-0.3}$	$-6.7^{+0.3}_{-0.3}$
$L(CH_4)$	-6.1	-6.1	-6.4	-6.7	$-5.2^{+1.2}_{-2.0}$	$-5.9^{+1.3}_{-2.0}$	$-7.4^{+1.4}_{-1.6}$	$-4.8^{+0.7}_{-0.7}$	$-5.1^{+0.6}_{-0.7}$	$-5.7^{+0.9}_{-1.2}$	$-4.6^{+0.9}_{-0.8}$	$-5.1^{+0.7}_{-0.8}$	$-6.0^{+0.9}_{-1.2}$	$-4.8^{+0.5}_{-0.5}$	$-5.1^{+0.4}_{-0.4}$	$-5.9^{+0.4}_{-0.5}$
$L(H_2O)$	-2.1	-5.7	$-2.5^{+0.8}_{-0.9}$	$-2.3^{+0.5}_{-0.5}$	$-2.1^{+0.3}_{-0.4}$	$-2.8^{+0.7}_{-0.8}$	$-2.2^{+0.4}_{-0.4}$	$-2.0^{+0.3}_{-0.4}$	$-2.5^{+0.8}_{-0.7}$	$-2.2^{+0.4}_{-0.4}$	$-2.0^{+0.3}_{-0.4}$	$-3.0^{+0.6}_{-0.6}$	$-2.2^{+0.4}_{-0.6}$	$-1.9^{+0.2}_{-0.3}$
$L(\delta_{H_2O})$	-2.0				...	$-2.3^{+1.4}_{-1.6}$	$-2.5^{+1.4}_{-1.5}$...	$-2.1^{+1.4}_{-1.6}$	$-2.6^{+1.4}_{-1.4}$...	$-2.3^{+1.4}_{-1.7}$	$-2.7^{+1.3}_{-1.4}$...	$-2.1^{+1.4}_{-1.8}$	$-3.0^{+1.1}_{-1.2}$
f_c	0.7				$0.6^{+0.2}_{-0.2}$	$0.7^{+0.2}_{-0.3}$	$0.8^{+0.1}_{-0.1}$
T_{eq} [K]	254				260^{+10}_{-9}	264^{+7}_{-7}	258^{+9}_{-8}	264^{+5}_{-5}	264^{+4}_{-4}	258^{+5}_{-6}	263^{+6}_{-7}	264^{+6}_{-5}	258^{+6}_{-7}	266^{+3}_{-3}	265^{+3}_{-3}	260^{+4}_{-4}
A_B	0.31				$0.24^{+0.10}_{-0.10}$	$0.19^{+0.08}_{-0.09}$	$0.26^{+0.09}_{-0.11}$	$0.19^{+0.07}_{-0.07}$	$0.19^{+0.05}_{-0.06}$	$0.26^{+0.07}_{-0.07}$	$0.20^{+0.08}_{-0.08}$	$0.20^{+0.06}_{-0.06}$	$0.26^{+0.08}_{-0.08}$	$0.17^{+0.04}_{-0.04}$	$0.18^{+0.04}_{-0.04}$	$0.23^{+0.05}_{-0.05}$
$L(P_0)$ [bar]	0.0				$-0.6^{+0.4}_{-0.3}$	$-0.4^{+0.3}_{-0.2}$	$-0.2^{+0.8}_{-0.4}$	$-0.4^{+0.3}_{-0.2}$	$-0.4^{+0.3}_{-0.2}$	$0.8^{+0.8}_{-0.6}$	$-0.5^{+0.4}_{-0.3}$	$-0.4^{+0.3}_{-0.2}$	$0.0^{+1.1}_{-0.1}$	$-0.4^{+0.3}_{-0.2}$	$-0.4^{+0.3}_{-0.2}$	$-0.4^{+0.8}_{-0.2}$
$L(P_{Op})$ [bar]	0.0				$-0.6^{+0.4}_{-0.3}$	$-0.4^{+0.3}_{-0.2}$	$-0.2^{+0.5}_{-0.4}$	$-0.4^{+0.3}_{-0.2}$	$-0.4^{+0.3}_{-0.2}$	$-0.0^{+0.3}_{-0.2}$	$-0.5^{+0.4}_{-0.3}$	$-0.4^{+0.3}_{-0.2}$	$-0.2^{+0.4}_{-0.2}$	$-0.4^{+0.3}_{-0.2}$	$-0.4^{+0.3}_{-0.2}$	$-0.4^{+0.3}_{-0.2}$
T_0 [K]	279				271^{+10}_{-9}	274^{+9}_{-8}	289^{+65}_{-14}	275^{+5}_{-5}	275^{+5}_{-5}	480^{+477}_{-161}	274^{+7}_{-7}	273^{+7}_{-6}	303^{+299}_{-23}	275^{+4}_{-4}	275^{+3}_{-3}	284^{+75}_{-8}
T_{Op} [K]	279				271^{+10}_{-9}	274^{+9}_{-8}	286^{+13}_{-11}	275^{+5}_{-5}	275^{+5}_{-5}	291^{+10}_{-6}	274^{+7}_{-7}	273^{+7}_{-6}	288^{+11}_{-9}	275^{+4}_{-4}	275^{+3}_{-3}	284^{+11}_{-7}
R_{pl} [R_{\oplus}]	1.0				$0.9^{+0.1}_{-0.1}$	$0.9^{+0.1}_{-0.1}$	$1.0^{+0.1}_{-0.1}$	$0.9^{+0.0}_{-0.0}$	$0.9^{+0.0}_{-0.0}$	$1.0^{+0.1}_{-0.1}$	$0.9^{+0.1}_{-0.1}$	$0.9^{+0.0}_{-0.0}$	$1.0^{+0.1}_{-0.1}$	$0.9^{+0.0}_{-0.0}$	$0.9^{+0.0}_{-0.0}$	$0.9^{+0.0}_{-0.0}$
$L(CO_2)$	-3.4				$-2.3^{+0.9}_{-0.9}$	$-2.9^{+0.6}_{-0.6}$	$-3.0^{+0.7}_{-0.8}$	$-2.7^{+0.7}_{-0.6}$	$-2.7^{+0.7}_{-0.6}$	$-3.2^{+0.5}_{-0.5}$	$-2.6^{+0.9}_{-0.8}$	$-2.7^{+0.6}_{-0.5}$	$-3.0^{+0.6}_{-0.6}$	$-2.8^{+0.5}_{-0.6}$	$-2.8^{+0.4}_{-0.4}$	$-2.7^{+0.4}_{-0.4}$
$L(O_3)$	-7.3	-5.9	-5.1	-5.3	$-5.6^{+0.7}_{-0.7}$	$-6.0^{+0.5}_{-0.5}$	$-6.2^{+0.6}_{-0.6}$	$-5.8^{+0.6}_{-0.6}$	$-5.9^{+0.4}_{-0.4}$	$-6.3^{+0.3}_{-0.3}$	$-5.7^{+0.7}_{-0.7}$	$-5.8^{+0.5}_{-0.5}$	$-6.2^{+0.5}_{-0.5}$	$-5.9^{+0.5}_{-0.5}$	$-5.9^{+0.3}_{-0.4}$	$-5.9^{+0.3}_{-0.4}$
$L(CH_4)$	-6.1	-6.1	-6.4	-6.7	$-4.9^{+1.1}_{-1.3}$	$-5.2^{+0.8}_{-1.3}$	$-6.0^{+1.3}_{-2.1}$	$-4.8^{+0.7}_{-0.7}$	$-4.9^{+0.5}_{-0.6}$	$-5.9^{+0.6}_{-0.8}$	$-4.8^{+0.9}_{-1.2}$	$-4.9^{+0.7}_{-0.7}$	$-5.6^{+0.8}_{-1.2}$	$-4.9^{+0.5}_{-0.6}$	$-4.9^{+0.4}_{-0.4}$	$-5.0^{+0.4}_{-0.6}$
$L(H_2O)$	-2.2	-5.7	$-2.7^{+0.8}_{-1.0}$	$-2.3^{+0.4}_{-0.7}$	$-2.2^{+0.5}_{-0.7}$	$-3.3^{+0.7}_{-0.7}$	$-2.3^{+0.4}_{-0.7}$	$-1.9^{+0.2}_{-0.3}$	$-3.1^{+0.9}_{-0.9}$	$-2.3^{+0.5}_{-0.8}$	$-2.0^{+0.3}_{-0.5}$	$-3.4^{+0.6}_{-0.6}$	$-2.2^{+0.4}_{-0.7}$	$-2.0^{+0.3}_{-0.7}$
$L(\delta_{H_2O})$	-2.0				...	$-2.4^{+1.5}_{-1.6}$	$-2.6^{+1.4}_{-1.5}$...	$-2.5^{+1.5}_{-1.6}$	$-3.3^{+1.2}_{-1.2}$...	$-2.4^{+1.6}_{-1.6}$	$-2.9^{+1.3}_{-1.3}$...	$-2.5^{+1.6}_{-1.6}$	$-2.8^{+1.5}_{-1.4}$
f_c	0.7				$0.4^{+0.2}_{-0.2}$	$0.6^{+0.2}_{-0.3}$	$0.4^{+0.4}_{-0.2}$
T_{eq} [K]	249				256^{+9}_{-8}	259^{+7}_{-7}	251^{+9}_{-8}	260^{+5}_{-5}	260^{+4}_{-4}	253^{+5}_{-6}	259^{+6}_{-6}	259^{+6}_{-5}	252^{+6}_{-7}	261^{+3}_{-3}	260^{+3}_{-3}	256^{+4}_{-5}
A_B	0.36				$0.28^{+0.09}_{-0.10}$	$0.25^{+0.08}_{-0.09}$	$0.34^{+0.08}_{-0.10}$	$0.23^{+0.06}_{-0.06}$	$0.24^{+0.05}_{-0.05}$	$0.32^{+0.06}_{-0.06}$	$0.25^{+0.07}_{-0.08}$	$0.25^{+0.06}_{-0.07}$	$0.32^{+0.07}_{-0.07}$	$0.23^{+0.04}_{-0.04}$	$0.24^{+0.04}_{-0.04}$	$0.29^{+0.05}_{-0.05}$

NOTE—Here, $L(\cdot)$ stands for $\log_{10}(\cdot)$. In columns two to five, we list the ground truth values for the view. If independent of the atmospheric pressure, we provide a single value. Otherwise, we provide ground truth values at 1 bar, 10^{-1} bar, 10^{-2} bar, and 10^{-3} bar where available. In the last twelve columns, we list the median and the 16% – 84% range (via +/– indices) of the parameter posteriors for all combinations of R (50, 100), S/N (10, 20), and retrieval model ($M_{C,CF}$, $M_{V,CF}$, $M_{V,CL}$). For H_2O , all listed posterior values correspond to the abundances at the pressure P_{Op} , where the atmosphere becomes optically thick.

Table A4. Numeric values for the EqC view posteriors shown in Figures A1 and A2.

Parameter	Ground Truths			Posteriors for $R = 50$ Spectra						Posteriors for $R = 100$ Spectra					
	Pressure Levels [bar]			LIFE _{ESIM} $S/N = 10$			LIFE _{ESIM} $S/N = 20$			LIFE _{ESIM} $S/N = 10$			LIFE _{ESIM} $S/N = 20$		
	1	10^{-1}	10^{-2}	$M_{C,CF}$	$M_{V,CF}$	$M_{V,CL}$	$M_{C,CF}$	$M_{V,CF}$	$M_{V,CL}$	$M_{C,CF}$	$M_{V,CF}$	$M_{V,CL}$	$M_{C,CF}$	$M_{V,CF}$	$M_{V,CL}$
$L(P_0)$ [bar]	0.0			-0.6 ^{+0.4} _{-0.4}	0.5 ^{+0.9} _{-0.7}	0.7 ^{+0.7} _{-0.8}	-0.4 ^{+0.4} _{-0.3}	-0.3 ^{+0.4} _{-0.2}	0.2 ^{+1.1} _{-0.6}	0.2 ^{+0.8} _{-0.7}	0.7 ^{+0.8} _{-0.7}	-0.4 ^{+0.3} _{-0.2}	-0.4 ^{+0.2} _{-0.2}	0.9 ^{+0.7} _{-0.7}	
$L(P_{Op})$ [bar]	0.0			-0.6 ^{+0.4} _{-0.4}	-0.0 ^{+0.4} _{-0.4}	0.1 ^{+0.3} _{-0.4}	-0.4 ^{+0.4} _{-0.3}	-0.4 ^{+0.3} _{-0.2}	-0.1 ^{+0.4} _{-0.3}	-0.1 ^{+0.3} _{-0.3}	-0.1 ^{+0.3} _{-0.3}	-0.4 ^{+0.3} _{-0.2}	-0.4 ^{+0.2} _{-0.2}	0.0 ^{+0.3} _{-0.3}	
T_0 [K]	280			281 ⁺¹⁰ ₋₉	331 ⁺³⁰³ ₋₄₆	408 ⁺³³¹ ₋₁₀₉	285 ⁺⁶ ₋₆	284 ⁺⁵ ₋₄	320 ⁺³⁸¹ ₋₃₁	451 ⁺⁴³¹ ₋₁₄₃	495 ⁺⁴⁸⁶ ₋₁₇₀	284 ⁺⁴ ₋₃	284 ⁺⁴ ₋₃	495 ⁺⁴⁸⁶ ₋₁₇₀	
T_{Op} [K]	280			281 ⁺¹⁰ ₋₉	284 ⁺¹⁰ ₋₇	289 ⁺¹⁰ ₋₈	285 ⁺⁶ ₋₆	284 ⁺⁵ ₋₄	291 ⁺⁹ ₋₇	289 ⁺¹⁰ ₋₇	293 ⁺⁸ ₋₇	284 ⁺⁴ ₋₃	284 ⁺⁴ ₋₃	293 ⁺⁸ ₋₇	
R_{p1} [R_{\oplus}]	1.0			0.9 ^{+0.1} _{-0.1}	0.9 ^{+0.1} _{-0.1}	1.0 ^{+0.1} _{-0.1}	0.9 ^{+0.0} _{-0.0}	0.9 ^{+0.0} _{-0.0}	1.0 ^{+0.1} _{-0.1}	1.0 ^{+0.1} _{-0.1}	1.0 ^{+0.0} _{-0.0}	0.9 ^{+0.0} _{-0.0}	0.9 ^{+0.0} _{-0.0}	1.0 ^{+0.0} _{-0.0}	
$L(CO_2)$	-3.4			-2.4 ^{+0.9} _{-0.9}	-3.7 ^{+0.9} _{-0.9}	-3.5 ^{+0.7} _{-0.7}	-2.7 ^{+0.8} _{-0.7}	-2.9 ^{+0.4} _{-0.5}	-3.1 ^{+0.6} _{-0.6}	-3.3 ^{+0.6} _{-0.6}	-3.3 ^{+0.4} _{-0.4}	-2.8 ^{+0.5} _{-0.6}	-2.8 ^{+0.3} _{-0.3}	-3.3 ^{+0.4} _{-0.4}	
$L(O_3)$	-7.4	-5.9	-5.0	-5.8 ^{+0.7} _{-0.7}	-6.6 ^{+0.5} _{-0.5}	-6.7 ^{+0.5} _{-0.4}	-6.0 ^{+0.6} _{-0.5}	-6.2 ^{+0.3} _{-0.4}	-6.4 ^{+0.5} _{-0.5}	-6.6 ^{+0.4} _{-0.4}	-6.5 ^{+0.2} _{-0.2}	-6.0 ^{+0.5} _{-0.5}	-6.1 ^{+0.3} _{-0.3}	-6.5 ^{+0.2} _{-0.2}	
$L(CH_4)$	-6.0	-6.1	-6.4	-4.9 ^{+1.2} _{-1.2}	-7.4 ^{+1.6} _{-1.5}	-7.5 ^{+1.5} _{-1.3}	-4.8 ^{+0.8} _{-0.7}	-5.2 ^{+0.5} _{-0.8}	-5.9 ^{+1.0} _{-1.3}	-6.3 ^{+0.9} _{-1.4}	-5.9 ^{+0.4} _{-0.4}	-4.8 ^{+0.5} _{-0.5}	-5.0 ^{+0.4} _{-0.4}	-5.9 ^{+0.4} _{-0.4}	
$L(H_2O)$	-2.1	-5.6	...	-2.5 ^{+0.7} _{-0.8}	-2.1 ^{+0.4} _{-0.4}	-2.1 ^{+0.3} _{-0.4}	-2.9 ^{+0.8} _{-0.7}	-2.1 ^{+0.4} _{-0.5}	-2.0 ^{+0.3} _{-0.4}	-1.9 ^{+0.3} _{-0.3}	-1.9 ^{+0.2} _{-0.2}	-3.1 ^{+0.6} _{-0.6}	-2.0 ^{+0.3} _{-0.3}	-1.9 ^{+0.2} _{-0.2}	
$L(\delta_{H_2O})$	-2.0			...	-2.6 ^{+1.5} _{-1.4}	-2.6 ^{+1.4} _{-1.4}	...	-2.5 ^{+1.5} _{-1.4}	-2.8 ^{+1.4} _{-1.3}	-3.1 ^{+1.4} _{-1.2}	-3.6 ^{+1.1} _{-1.0}	...	-2.5 ^{+1.6} _{-1.5}	-3.6 ^{+1.1} _{-1.0}	
f_c	0.7			0.5 ^{+0.2} _{-0.2}	0.5 ^{+0.2} _{-0.2}	0.6 ^{+0.1} _{-0.1}	0.7 ^{+0.1} _{-0.1}	0.7 ^{+0.1} _{-0.1}	
T_{eq} [K]	257			264 ⁺¹⁰ ₋₉	265 ⁺⁷ ₋₆	255 ⁺⁹ ₋₉	268 ⁺⁵ ₋₅	266 ⁺⁴ ₋₄	259 ⁺⁶ ₋₆	267 ⁺⁷ ₋₆	266 ⁺⁵ ₋₅	269 ⁺³ ₋₃	267 ⁺³ ₋₃	261 ⁺⁵ ₋₅	
A_B	0.27			0.19 ^{+0.11} _{-0.12}	0.17 ^{+0.08} _{-0.09}	0.29 ^{+0.09} _{-0.10}	0.14 ^{+0.07} _{-0.07}	0.17 ^{+0.05} _{-0.06}	0.25 ^{+0.07} _{-0.07}	0.27 ^{+0.08} _{-0.08}	0.27 ^{+0.08} _{-0.08}	0.13 ^{+0.05} _{-0.05}	0.15 ^{+0.04} _{-0.04}	0.23 ^{+0.05} _{-0.06}	
$L(P_0)$ [bar]	0.0			-0.5 ^{+0.4} _{-0.3}	0.8 ^{+0.7} _{-0.7}	0.6 ^{+0.8} _{-0.7}	-0.4 ^{+0.3} _{-0.3}	-0.2 ^{+0.8} _{-0.3}	0.8 ^{+0.7} _{-0.6}	0.8 ^{+0.7} _{-0.6}	0.8 ^{+0.7} _{-0.6}	-0.4 ^{+0.3} _{-0.2}	-0.4 ^{+0.2} _{-0.1}	0.4 ^{+1.0} _{-0.8}	
$L(P_{Op})$ [bar]	0.0			-0.5 ^{+0.4} _{-0.4}	-0.1 ^{+0.4} _{-0.4}	-0.0 ^{+0.4} _{-0.3}	-0.4 ^{+0.3} _{-0.3}	-0.4 ^{+0.3} _{-0.3}	0.1 ^{+0.3} _{-0.3}	0.1 ^{+0.3} _{-0.3}	-0.0 ^{+0.4} _{-0.3}	-0.4 ^{+0.3} _{-0.2}	-0.4 ^{+0.2} _{-0.1}	-0.1 ^{+0.3} _{-0.3}	
T_0 [K]	285			285 ⁺¹¹ ₋₁₀	406 ⁺³³⁰ ₋₁₁₀	389 ⁺³⁸⁷ ₋₉₀	288 ⁺⁶ ₋₅	288 ⁺⁶ ₋₆	474 ⁺³⁶⁸ ₋₁₄₄	468 ⁺⁴³⁵ ₋₁₅₅	381 ⁺⁴¹¹ ₋₈₅	289 ⁺⁴ ₋₃	287 ⁺⁴ ₋₃	381 ⁺⁴¹¹ ₋₈₅	
T_{Op} [K]	285			285 ⁺¹¹ ₋₁₀	284 ⁺¹¹ ₋₈	289 ⁺¹² ₋₈	288 ⁺⁶ ₋₅	285 ⁺⁷ ₋₇	290 ⁺⁸ ₋₆	290 ⁺⁸ ₋₆	294 ⁺⁹ ₋₇	289 ⁺⁴ ₋₃	287 ⁺⁴ ₋₃	294 ⁺⁹ ₋₇	
R_{p1} [R_{\oplus}]	1.0			0.9 ^{+0.1} _{-0.1}	1.0 ^{+0.1} _{-0.1}	1.0 ^{+0.1} _{-0.1}	0.9 ^{+0.0} _{-0.0}	1.0 ^{+0.1} _{-0.0}	1.0 ^{+0.1} _{-0.1}	1.0 ^{+0.1} _{-0.1}	1.0 ^{+0.0} _{-0.0}	0.9 ^{+0.0} _{-0.0}	0.9 ^{+0.0} _{-0.0}	1.0 ^{+0.0} _{-0.0}	
$L(CO_2)$	-3.4			-2.5 ^{+0.8} _{-0.8}	-3.5 ^{+0.8} _{-0.9}	-3.5 ^{+0.7} _{-0.7}	-2.7 ^{+0.7} _{-0.7}	-2.6 ^{+0.6} _{-0.6}	-3.4 ^{+0.5} _{-0.5}	-3.3 ^{+0.5} _{-0.5}	-3.3 ^{+0.5} _{-0.5}	-2.9 ^{+0.6} _{-0.6}	-2.7 ^{+0.3} _{-0.3}	-3.0 ^{+0.5} _{-0.5}	
$L(O_3)$	-7.3	-6.0	-5.0	-5.8 ^{+0.7} _{-0.6}	-6.5 ^{+0.5} _{-0.5}	-6.6 ^{+0.5} _{-0.4}	-5.9 ^{+0.6} _{-0.5}	-6.0 ^{+0.4} _{-0.4}	-6.6 ^{+0.3} _{-0.3}	-6.5 ^{+0.4} _{-0.4}	-6.3 ^{+0.4} _{-0.4}	-6.0 ^{+0.5} _{-0.5}	-5.9 ^{+0.3} _{-0.3}	-6.3 ^{+0.4} _{-0.3}	
$L(CH_4)$	-6.0	-6.1	-6.4	-5.0 ^{+1.1} _{-1.1}	-7.4 ^{+1.6} _{-1.6}	-7.4 ^{+1.5} _{-1.5}	-4.8 ^{+0.8} _{-0.7}	-5.1 ^{+0.7} _{-1.1}	-6.3 ^{+0.7} _{-1.0}	-6.3 ^{+0.6} _{-1.0}	-6.3 ^{+0.6} _{-1.0}	-4.9 ^{+0.6} _{-0.6}	-4.9 ^{+0.4} _{-0.4}	-5.6 ^{+0.7} _{-0.5}	
$L(H_2O)$	-2.1	-5.6	...	-2.6 ^{+0.8} _{-0.8}	-2.1 ^{+0.3} _{-0.4}	-2.0 ^{+0.3} _{-0.4}	-3.0 ^{+0.7} _{-0.7}	-1.9 ^{+0.3} _{-0.5}	-2.0 ^{+0.3} _{-0.3}	-1.9 ^{+0.3} _{-0.3}	-1.9 ^{+0.3} _{-0.3}	-3.1 ^{+0.6} _{-0.6}	-1.9 ^{+0.3} _{-0.3}	-1.8 ^{+0.3} _{-0.3}	
$L(\delta_{H_2O})$	-2.0			...	-2.6 ^{+1.6} _{-1.4}	-2.7 ^{+1.4} _{-1.4}	...	-2.6 ^{+1.5} _{-1.5}	-3.4 ^{+1.2} _{-1.2}	-3.1 ^{+1.4} _{-1.2}	-3.5 ^{+1.1} _{-0.9}	...	-2.6 ^{+1.6} _{-1.5}	-3.5 ^{+1.1} _{-0.9}	
f_c	0.7			0.4 ^{+0.2} _{-0.2}	0.6 ^{+0.1} _{-0.1}	0.5 ^{+0.1} _{-0.1}	0.6 ^{+0.2} _{-0.2}	0.6 ^{+0.2} _{-0.2}	
T_{eq} [K]	261			266 ⁺¹⁰ ₋₁₀	264 ⁺⁷ ₋₆	257 ⁺⁹ ₋₉	270 ⁺⁵ ₋₅	264 ⁺⁵ ₋₆	260 ⁺⁶ ₋₆	270 ⁺⁷ ₋₆	266 ⁺⁶ ₋₆	271 ⁺⁴ ₋₃	268 ⁺³ ₋₃	262 ⁺⁵ ₋₅	
A_B	0.23			0.16 ^{+0.12} _{-0.14}	0.19 ^{+0.07} _{-0.09}	0.27 ^{+0.09} _{-0.11}	0.11 ^{+0.07} _{-0.07}	0.19 ^{+0.07} _{-0.07}	0.24 ^{+0.07} _{-0.07}	0.26 ^{+0.08} _{-0.08}	0.26 ^{+0.08} _{-0.08}	0.10 ^{+0.05} _{-0.05}	0.13 ^{+0.04} _{-0.04}	0.22 ^{+0.06} _{-0.06}	

NOTE—Here, $L(\cdot)$ stands for $\log_{10}(\cdot)$. In columns two to five, we list the ground truth values for the view. If independent of the atmospheric pressure, we provide a single value. Otherwise, we provide ground truth values at 1 bar, 10^{-1} bar, 10^{-2} bar, and 10^{-3} bar where available. In the last twelve columns, we list the median and the 16% – 84% range (via +/- indices) of the parameter posteriors for all combinations of R (50, 100), S/N (10, 20), and retrieval model ($M_{C,CF}$, $M_{V,CF}$, $M_{V,CL}$). For H_2O , all listed posterior values correspond to the abundances at the pressure P_{Op} , where the atmosphere becomes optically thick.